A Geometrically Implicit Time-Stepping Method for Multibody Systems with Intermittent Contact

Nilanjan Chakraborty[⋆] **Stephen Berard**[†] **Srinivas Akella**[‡] **J. C. Trinkle**[†]

[⋆]School of Computer Science
Carnegie Mellon University
Pittsburgh, PA 15213

[‡]Department of Computer Science
University of North Carolina at Charlotte
Charlotte, NC 28223

[†]Department of Computer Science
Rensselaer Polytechnic Institute
Troy, NY 12180

Abstract

Accurate dynamic simulation with robust handling of intermittent contact is necessary for a wide range of robotics problems, including the design of parts feeding devices, manipulation/kinodynamic planning, and designing grasp strategies. In this paper we present an implicit time-stepping scheme for dynamic simulation of multi-body systems with intermittent contact by incorporating the contact constraints as a set of complementarity and algebraic equations within the dynamics model. We model each body as an intersection of convex inequalities and write the contact constraints as complementarity constraints between the contact force and a distance function dependent on the closest points on the bodies. The closest points satisfy a set of algebraic constraints obtained from the Karush-Kuhn-Tucker (KKT) conditions of the minimum distance problem. We prove that these algebraic equations and the complementarity constraints taken together ensure satisfaction of the contact constraints. This enables us to formulate a *geometrically* implicit time-stepping scheme (i.e., we do not need to approximate the distance function) as a nonlinear complementarity problem. The resulting time-stepper is therefore more accurate and does not rely on a closed form distance function. We demonstrate through example simulations the fidelity of this approach to analytical solutions and previously described simulation and experimental results.

Keywords: Multibody contact dynamics, dynamic simulation, complementarity, geometrically implicit time-stepper.

1 Introduction

The accurate prediction of object motions can enable the automatic planning and execution of tasks involving intermittent contact. Examples of robotics applications with contact include the design of local controllers for self-organizing systems (Klavins, 2007), synthesis and analysis of grasping and manipulation plans (Cherif and Gupta, 1999; Miller and Allen, 2000; Trinkle et al., 1993; Zumel and Erdmann, 1996), design and development of parts feeding devices (Song et al., 2004b), and design of assembly devices by vibrating plates (Vose et al., 2009). Due to the intermittency of contact and the presence of stick-slip frictional behavior, dynamic models of such multibody systems are inherently (mathematically) nonsmooth, and are thus difficult to integrate accurately. In fact, commercially available multibody dynamics software packages such as Adams (Software, 2012), have a difficult time simulating any system with unilateral contacts. Users expect to spend considerable effort in a trial-and-error search for good simulation parameters to obtain believable, not necessarily accurate, results.

The primary sources of stability and accuracy problems in dynamic simulation are polyhedral approximations of smooth bodies, the decoupling of collision detection from the solution of the dynamic time-stepping

subproblem, and approximations to the quadratic Coulomb friction model. This paper focuses on addressing the above problems by developing a geometrically implicit optimization-based time-stepper for dynamic simulation. More specifically, state-of-the-art geometrically explicit time-steppers (Liu and Wang, 2005; Song et al., 2004a; Stewart and Trinkle, 1996) use the contact point information obtained from a collision detection algorithm at the beginning of the time-step to compute the state of the system at the end of the time-step (by solving a dynamics time step subproblem) without modifying the contact information. In other words, in geometrically explicit time-steppers, the collision detection and the dynamic simulation time-step are decoupled. Thus, state-of-the-art time-steppers can be viewed as *explicit* methods with respect to geometric information. This may lead to the contact constraints not being satisfied at the end of the time step (e.g., inter-penetration of the objects may occur). In contrast, geometrically implicit methods must solve the collision detection problem and dynamic time-stepping problem simultaneously. We develop the first time-stepping method that is implicit in the geometric information (when the distance function is not available in closed form) by incorporating body geometry in the dynamic time-stepping subproblem. Our formulation solves the collision detection and dynamic stepping problems simultaneously, i.e., we obtain the contact points and the state of the system at the end of the time-step so that the contact constraints at the end of the time step are satisfied.

We illustrate the combined effects of geometric approximation and decoupling of collision detection from dynamic time-stepping during dynamic simulation using a simple example. Consider the planar problem of a uniform disc rolling on a horizontal support surface. For this problem, the exact analytical solution is known, *i.e.,* the disc will roll at constant speed *ad infinitum.* However, when the disc is approximated by a uniform regular polygon, energy is lost due to: a) collisions between the vertices and the support surface, b) contact sliding that is resisted by friction, and c) artificial impulses generated by the approximate distance function that is to be satisfied at the end of the time-step. We simulated this example in dVC (Berard et al., 2007) using the Stewart-Trinkle time-stepping algorithm (Stewart and Trinkle, 1996). The plots in Figure 1 show the reduction of kinetic energy over time caused by the accumulation of these effects. Figure 1a shows that with a fixed time-step (of 0.01 seconds for the figure), as the number of edges is increased, the energy loss decreases. However, the decrease in energy loss approaches a limit (determined by the size of the time-step). As can be seen in Figure 1a, the loss of energy when the disc is approximated by 1000 vertices is indistinguishable from a ten times finer approximation, when the disc is approximated by $10,000$ vertices. Figure 1b shows that for a fixed number of vertices (1000 in this example), as the time-step decreases further from $t = 0.01$, the energy loss decreases. However, even with the decrease in time-step an energy loss limit is reached. The plots for $h = 0.001$ and $h = 0.0001$ are indistinguishable. These plots demonstrate that the discretization of geometry and linearization of the distance function lead to the artifact of loss of energy in the simulations.

To address these issues and related problems, we develop a geometrically implicit time-stepping method for dynamic simulation. The key idea in developing the time-stepping method is to incorporate the contact constraints in the dynamics model as a set of complementarity and algebraic equations. We model each body as an intersection of convex inequalities and write the contact constraints as complementarity constraints between the contact force and a distance function dependent on the closest points on the bodies. The closest points satisfy a set of algebraic equations obtained from the KKT conditions of the minimum distance problem. We use a backward Euler time discretization, and the resulting subproblem at each time-step is a mixed nonlinear complementarity problem. Since we solve for the contact points, contact normal, and contact force at the end of the time-step simultaneously, we call our time-stepping scheme a *geometrically implicit* time-stepping scheme. We first present the method for rigid bodies and then extend it to locally compliant or quasi-rigid bodies, where each body consists of a rigid core surrounded by a thin compliant shell (Pauly et al., 2004; Song et al., 2001; Song and Kumar, 2003; Song et al., 2004a). Our method also takes into consideration other important nonlinear elements such as quadratic Coulomb friction. Although in the development of our time-stepping model we have assumed the objects to be convex, our method can also be used for non-convex objects that are described as an union of convex objects. We illustrate this using an example grasping task (Section 6.4).

This paper combines and extends our earlier work in (Chakraborty et al., 2007a) and (Chakraborty et al., 2007b). It is organized as follows: In Section 2 we give a brief overview of the literature in dynamic simulation related to our present work. In Section 3, we present both the continuous and discrete time

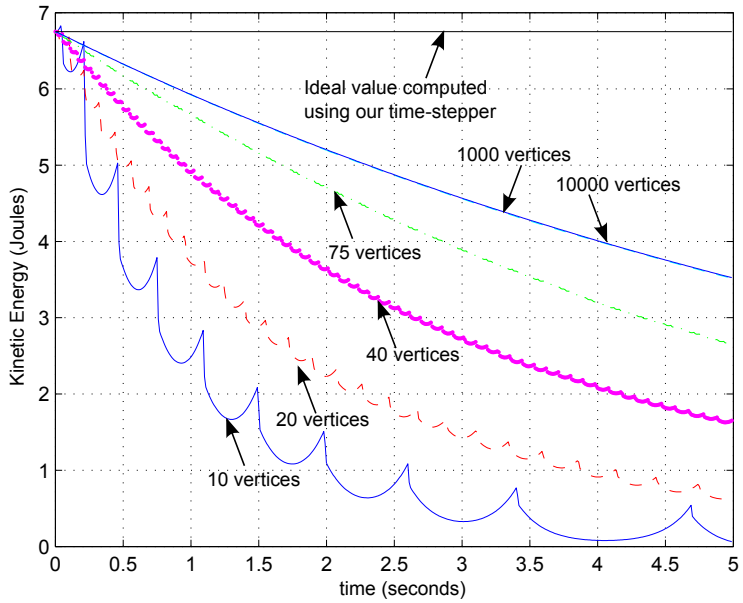

(a) As the number of vertices of the "rolling" polygon increases, the energy loss decreases. The computed value obtained by our time-stepper using an implicit surface description of the disc is the horizontal line at the top. The time step used is 0.01 second.

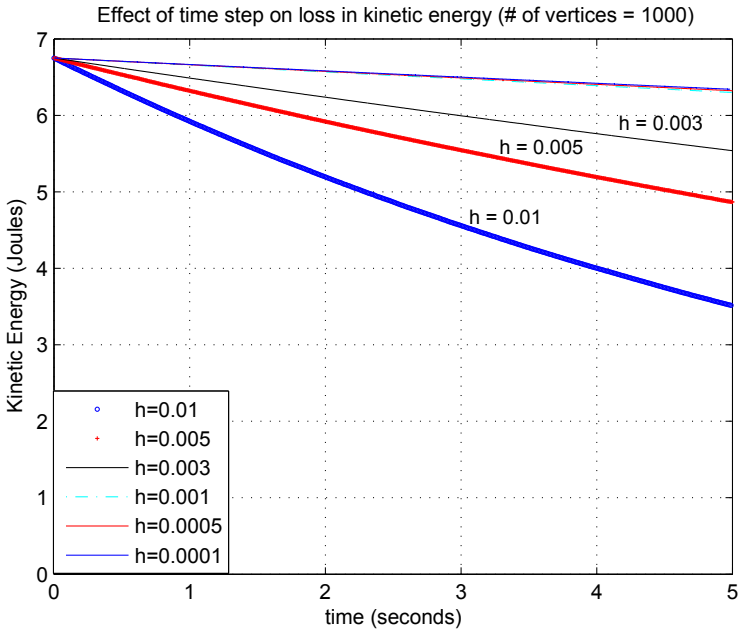

(b) For a given number of vertices, the energy loss decreases with decreasing step size, up to a limit. In this case, the limit is approximately 0.001 second (the top curve consists of the plots for time steps of 0.001, 0.0005, and 0.0001, which are indistinguishable).

Figure 1: For a disc rolling on a surface, plots of the reduction of kinetic energy over time caused by approximating the disc as a uniform regular polygon.

dynamics model for multi-rigid-body systems with an ellipsoidal dry friction law. In Section 4, we develop a new formulation of the non-penetration condition (i.e., contact constraints) assuming the bodies to be rigid. Thereafter, in Section 5, we modify these contact constraints to include compliant contacts with limits on the maximum allowable deflection. The discrete time dynamics model along with the contact constraints form a mixed nonlinear complementarity problem at each time-step. In Section 6, we give examples for the rigid and locally compliant methods that validate and elucidate our time-stepping scheme. In Section 6.4, we apply our dynamic simulation algorithms to study in simulation a grasping experiment performed by (Brost and Christiansen, 1996). Finally in Section 8, we present our conclusions and lay out the future work.

2 Related Work

Dynamics of multi-rigid-body systems with unilateral contacts can be modeled as differential algebraic equations (DAE) (Haug et al., 1986) if the contact interactions (sliding, rolling, or separating) at each contact are known. However, in general, the contact interactions are not known *a priori*, but rather are discovered as part of the solution process. To handle the many possibilities in a rigorous theoretical and computational framework, the model is formulated as a differential complementarity problem (Cottle et al., 1992; Trinkle et al., 1997). The problem is solved using a time-stepping scheme and the resultant system of equations to be solved at each step is a (linear/nonlinear) complementarity problem.

Let $\mathbf{u} \in \mathbb{R}^{n_1}$, $\mathbf{v} \in \mathbb{R}^{n_2}$ and let $g : \mathbb{R}^{n_1} \times \mathbb{R}^{n_2} \to \mathbb{R}^{n_1}$, $f : \mathbb{R}^{n_1} \times \mathbb{R}^{n_2} \to \mathbb{R}^{n_2}$ be two vector functions and the notation $\mathbf{0} \leq \mathbf{x} \perp \mathbf{y} \geq \mathbf{0}$ imply that $\mathbf{x}$ is orthogonal to $\mathbf{y}$ and each component of the vectors is non-negative.

Definition 1. (Pang and Facchinei, 2003) The differential (or dynamic) complementarity problem is to find $\mathbf{u}$ and $\mathbf{v}$ satisfying

$$\begin{aligned} \dot{\mathbf{u}} &= g(\mathbf{u}, \mathbf{v}) \\ 0 \leq \mathbf{v} \ &\perp \ f(\mathbf{u}, \mathbf{v}) \geq 0 \end{aligned}$$

Definition 2. The mixed complementarity problem is to find $\mathbf{u}$ and $\mathbf{v}$ satisfying

$$\begin{aligned} g(\mathbf{u}, \mathbf{v}) &= 0 \\ 0 \leq \mathbf{v} \ &\perp \ f(\mathbf{u}, \mathbf{v}) \geq 0 \end{aligned}$$

If the functions f and g are linear the problem is called a mixed linear complementarity problem (MLCP), otherwise, the problem is called a mixed nonlinear complementarity problem (MNCP).

The three primary modeling approaches for multibody systems with unilateral contacts are based on three different assumptions about the flexibility of the bodies. The assumptions from most to least realistic (and most to least computationally complex) are: 1) the bodies are fully deformable, 2) the bodies have rigid cores surrounded by compliant material, 3) the bodies are fully rigid. The first assumption leads to finite element approaches, for which one must solve very large difficult complementarity problems or variational inequalities at each time step. The second assumption leads to smaller subproblems that can be solved more easily (Pauly et al., 2004; Song et al., 2004a), but suitable values of the parameters of the compliant layer can be difficult to determine. The assumption of rigid bodies leads to the smallest subproblems and avoids the problem of determining material deformation properties.

Independent of the rigidity assumptions of the bodies, the methods developed to date for dynamic simulation have one problem in common that fundamentally limits their accuracy – they are not implicit with respect to the relevant geometric information. For example, at the current state, a collision detection routine is called to determine separation or penetration distances between the bodies, but this information is not incorporated as a function of the unknown future state at the end of the current time step. A goal of a typical time-stepping scheme is to guarantee consistency of the dynamic equations and all model constraints at the end of each time step. However, since the geometric information at the end of the current time step is approximated from that at the start of the time step, the solution will be in error.

Early time-steppers used linear approximations of the local geometry at the current time (Anitescu et al., 1996; Stewart and Trinkle, 1996). Thus each contact was treated as a point on a plane or a line on a (non-parallel) line and these entities were assumed constant for the duration of the time step. Besides being

insufficiently accurate in some applications, some unanticipated side-effects arose (Berard et al., 2004, 2010; Egan et al., 2003; Nguyen and Trinkle, 2010). The linear approximation leads to a representation of the local portion of collision-free configuration space by a convex subset of the actual non-convex set. Thus, it is possible to have *phantom collisions* where collisions are detected even though there are none (Nguyen and Trinkle, 2010).

Increased accuracy can be obtained in explicit schemes by including curvature information. This was done by (Liu and Wang, 2005) and (Pfeiffer and Glocker, 1996) by incorporating kinematic differential equations of rolling contact (Montana, 1998). Outside the complementarity formalism, (Kry and Pai, 2003) and (Baraff, 1990) also make use of the contact kinematics equations in dynamic simulations of parametric and implicit surface objects respectively.

The method of (Tzitzouris, 2001) is the only geometrically implicit method developed to date, but unfortunately it requires that the distance function between the bodies and two levels of derivatives be available in closed form. However, it is possible that this method could run successfully after replacing the closed-form distance functions with calls to collision detection algorithms and replacing derivatives with difference approximations from multiple collision detection calls, but polyhedral approximations common to most collision detection packages would generate very noisy derivatives. To our knowledge, such an implementation has not been attempted. One other problem with Tzitzouris' method is that it adapts its step size to precisely locate every collision time. While this is a good way to avoid interpenetration at the end of a time step, it has the undesirable side-effect of forcing the step size to be unreasonably small when there are many interacting bodies (Mirtich, 1996). The method we propose does not suffer from this problem.

2.1 Collision Modeling for Nominally Rigid Body Systems

Frictional collisions between rigid bodies have a long history in mechanics (Keller, 1986; Routh, 1905). Here, we give an overview of the basic approaches and refer the reader to a recent survey article (Gilardi and Sharif, 2002) for a more comprehensive review. There are two primary approaches to modeling collisions: coefficient of restitution based approaches and force based methods. In the former, the process of energy transfer and dissipation during collision is modeled by various coefficients relating the velocity (or impulses) before contact to that after contact. However, the extension of these concepts to situations with multiple contacts is not straightforward (see (Jia et al., 2013; Seghete and Murphey, 2010, 2012) for recent progress in this direction). The force based approaches use a compliant contact model to compute the contact forces where the contact compliance is modeled as a (linear/nonlinear) spring-damper system. In the simplest model, known as the Kelvin-Voigt model or linear spring-damper model, the normal contact force is given by a linear function of the deformation and the rate of deformation ($F = k\delta + c\dot{\delta}$), i.e., the flexibility of the body is lumped as a linear spring (with spring constant k) and damper (with damping coefficient c). The limitations of the linear model are documented in (Gilardi and Sharif, 2002). Hertz introduced a nonlinear model of the form $F = k\delta^n$, where n is a constant (Johnson, 1985). This model was extended by (Hunt and Crossley, 1975) to a nonlinear spring-damper model of the form $F = k\delta^n + c\delta^p\dot{\delta}^q$, where p, q are constants. The models presented above are believed to be of increasing accuracy but there are more unknown constants dependent on geometry of the objects and material properties that have to be determined experimentally (except for some simple cases). This is a general feature of all proposed contact compliance models. In (Wang and Kumar, 1994) a continuum model of the deformations at each contact is used. In (Song and Kumar, 2003), the authors have used a 3D linear distributed contact model to compute the contact forces. In this paper we use a lumped 3D linear spring-damper to model the contact compliance similar to (Kraus et al., 1997). However, we note that we could have replaced this with a lumped nonlinear model if required. We use an elliptic dry friction law (Goyal et al., 1991a,b; Howe and Cutkosky, 1996; Trinkle and Pang, 1997; Trinkle et al., 2001) that is a generalization of Coulomb's friction law to model the friction at the contact (please see the "Friction Model" in Section 3 for the actual friction law used).

3 Dynamic Model for Multibody Systems

In complementarity methods, the instantaneous equations of motion of a multi-rigid-body system consist of five parts: (a) Newton-Euler equations, (b) Kinematic map relating the generalized velocities to the linear

and angular velocities, (c) Equality constraints to model joints, (d) Normal contact condition to model intermittent contact, and (e) Friction law. Parts (a) and (b) form a system of ordinary differential equations, (c) is a system of (nonlinear) algebraic equations, (d) is given by a system of complementarity constraints, and (e) can be written as a system of complementarity constraints for Coulomb friction law using the maximum work dissipation principle. In this paper we use a more general elliptic dry friction law (Trinkle et al., 2001). Thus, the dynamic model is a *differential complementarity problem* (DCP). To solve this system of equations, we set up a time-stepping scheme and solve a complementarity problem at each time step. We present below the instantaneous-time formulation as well as an Euler time-stepping scheme. To simplify the exposition, we ignore the presence of joints or bilateral constraints in the following discussion. However, all of the discussion below holds in the presence of bilateral constraints.

To describe the dynamic model mathematically, we first introduce some notation. Let $\mathbf{q}_j$ be the position and orientation of body j in an inertial frame and $\boldsymbol{\nu}_j$ be the concatenated vector of linear ($\mathbf{v}$) and angular ($\boldsymbol{\omega}$) velocities. The generalized coordinates $\mathbf{q}$, and generalized velocity $\boldsymbol{\nu}$ of the whole system are formed by concatenating $\mathbf{q}_j$ and $\boldsymbol{\nu}_j$ respectively. Let $\lambda_{i\mathrm{n}}$ be the normal contact force at the ith contact and $\boldsymbol{\lambda}_\mathrm{n}$ be the concatenated vector of the normal contact forces. Let $\lambda_{i\mathrm{t}}$ and $\lambda_{i\mathrm{o}}$ be the orthogonal components of the friction force on the tangential plane at the ith contact and $\boldsymbol{\lambda}_\mathrm{t}$, $\boldsymbol{\lambda}_\mathrm{o}$ be the respective concatenated vectors. Let $\lambda_{i\mathrm{r}}$ be the frictional moment about the ith contact normal and $\boldsymbol{\lambda}_\mathrm{r}$ be the concatenated vector of the frictional moments. Let n_b be the number of bodies and n_c be the number of contacts. Throughout the paper, we consider vectors as column vectors and for any two vectors $\mathbf{x}, \mathbf{y}$, the notation $[\mathbf{x}, \mathbf{y}]$ denotes horizontal concatenation and the notation $[\mathbf{x}; \mathbf{y}]$ denotes vertical concatenation. The instantaneous dynamic model can then be written as follows:

Newton-Euler Equations of Motion:

$$\mathbf{M}(\mathbf{q})\dot{\boldsymbol{\nu}} = \mathbf{W}_\mathrm{n}\boldsymbol{\lambda}_\mathrm{n} + \mathbf{W}_\mathrm{t}\boldsymbol{\lambda}_\mathrm{t} + \mathbf{W}_\mathrm{o}\boldsymbol{\lambda}_\mathrm{o} + \mathbf{W}_\mathrm{r}\boldsymbol{\lambda}_\mathrm{r} + \boldsymbol{\lambda}_\mathrm{app} + \boldsymbol{\lambda}_\mathrm{vp} \tag{1}$$

where $\mathbf{M}(\mathbf{q})$ is the inertia tensor, $\boldsymbol{\lambda}_\mathrm{app}$ is the vector of external forces, $\boldsymbol{\lambda}_\mathrm{vp}$ is the vector of Coriolis and centripetal forces, $\mathbf{W}_\mathrm{n}$, $\mathbf{W}_\mathrm{t}$, $\mathbf{W}_\mathrm{o}$, and $\mathbf{W}_\mathrm{r}$ are dependent on $\mathbf{q}$ and map the normal contact forces, frictional contact forces, and frictional moments to the body reference frame.

Kinematic Map:

$$\dot{\mathbf{q}} = \mathbf{G}(\mathbf{q})\boldsymbol{\nu} \tag{2}$$

where $\mathbf{G}$ is the matrix mapping the generalized velocity of the body to the time derivative of the position and orientation. The Jacobian $\mathbf{G}$ may be a non-square matrix (*e.g.*, using a unit quaternion to represent orientation) but $\mathbf{G}^T\mathbf{G} = \mathbf{I}$.

Nonpenetration Constraints: The normal contact constraint for the ith contact is

$$0 \le \lambda_{i\mathrm{n}} \perp \psi_{i\mathrm{n}}(\mathbf{q}, t) \ge 0 \tag{3}$$

where $i = 1, \ldots, n_c$, $\psi_{i\mathrm{n}}$ is a signed distance function or *gap function* for the ith contact with the property $\psi_{i\mathrm{n}}(\mathbf{q}, t) > 0$ for separation, $\psi_{i\mathrm{n}}(\mathbf{q}, t) = 0$ for touching, and $\psi_{i\mathrm{n}}(\mathbf{q}, t) < 0$ for interpenetration. The above gap function is defined in the configuration space of the system. Note that there is usually no closed form expression for $\psi_{i\mathrm{n}}(\mathbf{q}, t)$.

Friction Model: The friction model is a generalization of Coulomb's friction law and is based on the maximum power dissipation principle.

$$(\lambda_{i\mathrm{t}},\ \lambda_{i\mathrm{o}},\ \lambda_{i\mathrm{r}}) \in \underset{(\lambda'_{i\mathrm{t}}, \lambda'_{i\mathrm{o}}, \lambda'_{i\mathrm{r}}) \in \mathbf{F}_i}{\arg\max} \left(-(v_{i\mathrm{t}}\lambda'_{i\mathrm{t}} + v_{i\mathrm{o}}\lambda'_{i\mathrm{o}} + v_{ir}\lambda'_{i\mathrm{r}})\right) \tag{4}$$

where $i = 1, \ldots, n_c$, v_{it} and v_{io} are the tangential components of the relative velocity at contact i, v_{ir} is the relative angular velocity about the normal at the contact, and $\mathbf{F}_i(\lambda_{in}, \mu_i)$ denotes the friction cone at contact i:

$$\mathbf{F}_i(\lambda_{in}, \mu_i) = \left\{ (\lambda_{it},\ \lambda_{io},\ \lambda_{ir}) : \left(\frac{\lambda_{it}}{e_{it}}\right)^2 + \left(\frac{\lambda_{io}}{e_{io}}\right)^2 + \left(\frac{\lambda_{ir}}{e_{ir}}\right)^2 \leq \mu_i^2 \lambda_{in}^2 \right\} \tag{5}$$

where e_{it}, e_{io}, and e_{ir} are given positive constants defining the friction ellipsoid and μ_i is the coefficient of friction at the ith contact (Howe and Cutkosky, 1996; Trinkle and Pang, 1997). Equation (5) is the elliptic dry friction condition suggested in (Howe and Cutkosky, 1996) based upon evidence from a series of contact experiments. This model states that among all the possible contact forces and moments that lie within the friction ellipsoid (given by Equation (5)), the forces and moment that maximize the power dissipation at the contact (due to friction) are selected.

Time-Stepping Formulation: We use a velocity-level formulation and an Euler time-stepping scheme to discretize the above system of equations. Let t_ℓ denote the current time, h be the time step. Use the superscripts ℓ and $\ell+1$ to denote quantities at the beginning and end of the ℓth time step respectively. Using $\dot{\boldsymbol{\nu}}^{\ell+1} \approx (\boldsymbol{\nu}^{\ell+1} - \boldsymbol{\nu}^{\ell})/h$ and $\dot{\mathbf{q}}^{\ell+1} \approx (\mathbf{q}^{\ell+1} - \mathbf{q}^{\ell})/h$, and writing in terms of the impulses we get the following discrete time system.

$$\begin{aligned}
\mathbf{M}^{\ell}\boldsymbol{\nu}^{\ell+1} &= \mathbf{M}^{\ell}\boldsymbol{\nu}^{\ell} + h(\mathbf{W}_{\mathrm{n}}\boldsymbol{\lambda}_{\mathrm{n}}^{\ell+1} + \mathbf{W}_{\mathrm{t}}\boldsymbol{\lambda}_{\mathrm{t}}^{\ell+1} + \mathbf{W}_{\mathrm{o}}\boldsymbol{\lambda}_{\mathrm{o}}^{\ell+1} + \mathbf{W}_{\mathrm{r}}\boldsymbol{\lambda}_{\mathrm{r}}^{\ell+1} + \boldsymbol{\lambda}_{\mathrm{app}}^{\ell} + \boldsymbol{\lambda}_{\mathrm{vp}}^{\ell}) \\
\mathbf{q}^{\ell+1} &= \mathbf{q}^{\ell} + h\mathbf{G}\boldsymbol{\nu}^{\ell+1} \\
0 \leq h\boldsymbol{\lambda}_{\mathrm{n}}^{\ell+1} &\perp \psi_{\mathrm{n}}(\mathbf{q}^{\ell+1}) \geq 0 \\
h(\lambda_{it},\ \lambda_{io},\ \lambda_{ir}) &\in \underset{h(\lambda'_{it},\lambda'_{io},\lambda'_{ir}) \in h\mathbf{F}_i}{\arg\max} \left(-h(v_{it}\lambda'_{it} + v_{io}\lambda'_{io} + v_{ir}\lambda'_{ir})\right)
\end{aligned} \tag{6}$$

The argmax formulation of the friction law has a useful alternative formulation (Trinkle et al., 2001):

$$\begin{aligned}
0 &= \mathbf{E}_t^2\mathbf{U}\mathbf{p}_{\mathrm{n}} \circ \mathbf{W}_{\mathrm{t}}^T\boldsymbol{\nu}^{\ell+1} + \mathbf{p}_{\mathrm{t}} \circ \boldsymbol{\sigma} \\
0 &= \mathbf{E}_o^2\mathbf{U}\mathbf{p}_{\mathrm{n}} \circ \mathbf{W}_{\mathrm{o}}^T\boldsymbol{\nu}^{\ell+1} + \mathbf{p}_{\mathrm{o}} \circ \boldsymbol{\sigma} \\
0 &= \mathbf{E}_r^2\mathbf{U}\mathbf{p}_{\mathrm{n}} \circ \mathbf{W}_{\mathrm{r}}^T\boldsymbol{\nu}^{\ell+1} + \mathbf{p}_{\mathrm{r}} \circ \boldsymbol{\sigma} \\
0 &\leq (\mathbf{U}\mathbf{p}_{\mathrm{n}}) \circ (\mathbf{U}\mathbf{p}_{\mathrm{n}}) - \left(\mathbf{E}_{\mathrm{t}}^2\right)^{-1}(\mathbf{p}_{\mathrm{t}} \circ \mathbf{p}_{\mathrm{t}}) - \left(\mathbf{E}_{\mathrm{o}}^2\right)^{-1}(\mathbf{p}_{\mathrm{o}} \circ \mathbf{p}_{\mathrm{o}}) - \left(\mathbf{E}_{\mathrm{r}}^2\right)^{-1}(\mathbf{p}_{\mathrm{r}} \circ \mathbf{p}_{\mathrm{r}}) \perp \boldsymbol{\sigma} \geq 0
\end{aligned} \tag{7}$$

where $\circ$ connotes the Hadamard product, the impulse $\mathbf{p}_{(\cdot)} = h\boldsymbol{\lambda}_{(\cdot)}$, the matrices $\mathbf{E}_{\mathrm{t}}$, $\mathbf{E}_{\mathrm{o}}$, $\mathbf{E}_{\mathrm{r}}$, and $\mathbf{U}$ are diagonal with ith diagonal element equal to e_{it}, e_{io}, e_{ir}, and μ_i respectively, $\boldsymbol{\sigma}$ is a concatenated vector of the Lagrange multipliers arising from the Fritz John optimality conditions of the argmax formulation. Each component of $\boldsymbol{\sigma}$ (i.e., σ_i) is the magnitude of the slip velocity at contact i. The vectors $\mathbf{p}_n$, $\mathbf{p}_t$, and $\mathbf{p}_o$ are each formed by concatenating the magnitude of the normal contact impulse and the orthogonal components of the tangential contact impulse at all the contacts. The vector $\mathbf{p}_r$ is formed by concatenating the magnitude of the contact moments about the contact normal.

Equation (6), which is to be solved at each time step, is either an LCP or an NCP depending on the time of evaluation of $\mathbf{W}_{(\cdot)}$, the approximation used for $\psi_{\mathrm{n}}(\mathbf{q}^{\ell+1})$, and the representation of the friction model. If we evaluate $\mathbf{W}_{(\cdot)}$ at $\ell+1$, use a quadratic friction law (Equation (7)), and use $\psi_{\mathrm{n}}(\mathbf{q}^{\ell+1})$, we have a geometrically implicit NCP formulation ensuring that the contact conditions are satisfied at the end of the time step. However, evaluating $\psi_{\mathrm{n}}(\mathbf{q}^{\ell+1})$ is possible only if we have a closed form expression for the distance function, which we do not have in general. Instead, in the next section we formulate the gap function between the closest points as a set of algebraic equations, and subsequently extend the formulation to include compliance.

4 Contact Constraints for Rigid Bodies

In this section we rewrite the contact condition (Equation (3)) as a complementarity condition in the work space, combine it with an optimization problem to find the closest points, and prove that the resultant

system of equations ensures that the contact constraints are satisfied. Let us consider the ith contact. For ease of exposition, we first present the case where each object is a convex object described by a single implicit surface. A more general formulation where each object is described by an intersection of implicit surfaces is given in Section 4.3.

4.1 Objects Described by a Single Convex Function

Let the two objects be defined by $\mathcal{C}^2$ convex (i.e., twice differentiable with continuous second derivatives) functions $f(\boldsymbol{\xi}_1) \leq 0$ and $g(\boldsymbol{\xi}_2) \leq 0$ respectively, where $\boldsymbol{\xi}_1$ and $\boldsymbol{\xi}_2$ are the coordinates of points in the two objects. Let $\mathbf{a}_1$ and $\mathbf{a}_2$ be the closest points on the two objects. The equation of an implicit surface has the property that for any point $\mathbf{x}$, the point lies inside the object for $f(\mathbf{x}) < 0$, on the object surface for $f(\mathbf{x}) = 0$, and outside the object for $f(\mathbf{x}) > 0$. Thus, we can define the gap function in the work space as either $f(\mathbf{a}_2)$ or $g(\mathbf{a}_1)$ and write the complementarity conditions as either one of the following two conditions:

$$\begin{aligned} 0 \leq \lambda_{in} \perp f(\mathbf{a}_2) \geq 0 \\ 0 \leq \lambda_{in} \perp g(\mathbf{a}_1) \geq 0 \end{aligned} \tag{8}$$

where $\mathbf{a}_1$ and $\mathbf{a}_2$ are given by a solution to the following minimization problem:

$$(\mathbf{a}_1,\ \mathbf{a}_2) = \arg\min_{\boldsymbol{\xi}_1, \boldsymbol{\xi}_2} \left\{ \|\boldsymbol{\xi}_1 - \boldsymbol{\xi}_2\|^2 : f(\boldsymbol{\xi}_1) \leq 0,\ \ g(\boldsymbol{\xi}_2) \leq 0 \right\}. \tag{9}$$

The Karush-Kuhn-Tucker (KKT) optimality conditions ((Chakraborty et al., 2008)) that the solutions $\mathbf{a}_1$ and $\mathbf{a}_2$ of Equation (9) must satisfy are given by the following system of algebraic equations:

$$\begin{aligned} \mathbf{a}_1 - \mathbf{a}_2 &= -\hat{l}_1 \nabla f(\mathbf{a}_1) \\ \mathbf{a}_1 - \mathbf{a}_2 &= \hat{l}_2 \nabla g(\mathbf{a}_2) \\ f(\mathbf{a}_1) + s_1 &= 0 \\ g(\mathbf{a}_2) + s_2 &= 0 \\ 0 \leq \hat{l}_1 &\perp s_1 \geq 0 \\ 0 \leq \hat{l}_2 &\perp s_2 \geq 0 \end{aligned} \tag{10}$$

where $\hat{l}_1$ and $\hat{l}_2$ are the Lagrange multipliers and s_1 and s_2 are the slack variables. After eliminating the slack variables, the system of Equations (10) can be rewritten as the following equivalent system:

$$\mathbf{a}_1 - \mathbf{a}_2 = -\hat{l}_1 \nabla f(\mathbf{a}_1) \tag{11}$$

$$\hat{l}_1 \nabla f(\mathbf{a}_1) = -\hat{l}_2 \nabla g(\mathbf{a}_2) \tag{12}$$

$$0 \leq \hat{l}_1 \perp -f(\mathbf{a}_1) \geq 0 \tag{13}$$

$$0 \leq \hat{l}_2 \perp -g(\mathbf{a}_2) \geq 0. \tag{14}$$

The geometric meaning of Equations (11) and (12) is that the normals to the two surfaces at their closest points are parallel to the line joining the closest points. The solution to the system of Equations (11) to (14) gives the closest point when the two objects are separate. However, when $\mathbf{a}_1 = \mathbf{a}_2$, both Lagrange multipliers are forced to become 0 (since both $\|\nabla f(\mathbf{a}_1)\| > 0$ and $\|\nabla g(\mathbf{a}_2)\| > 0$) and there are multiple solutions to the KKT conditions. The solution is either the touching point of the two surfaces or a point lying in the intersection set of the two objects (see Figure 2). The complementarity conditions in Equation (8) ensure that the points in the interior of the objects are not feasible solution to the overall problem. However, the points on the intersecting surface as well as the touching points are valid solutions to Equations (11)–(14) and (8). Thus, as written, Equations (11)–(14) and (8) do not guarantee non-penetration. We want to form a system of equations that is equivalent to the KKT conditions (Equations (11)–(14)) when the distance between the objects is non-negative but only gives the touching solution when the distance is zero (middle case in Figure 2 with parallel surface normals).

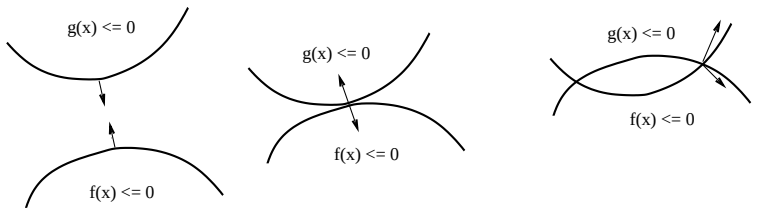

Figure 2: Three contact cases: (a) objects are separate, (b) objects are touching, (c) objects are intersecting. The arrows indicate the surface normals at the closest points.

Proposition 1. *Equations* (15)–(18) *are equivalent to the KKT conditions when the distance between the objects is non-negative. Moreover, when combined with the complementarity condition in Equation* (19)*, it gives only the touching solution when the distance between the objects is zero.*

$$\mathbf{a}_1 - \mathbf{a}_2 = -l_1 \nabla f(\mathbf{a}_1) \tag{15}$$
$$\nabla f(\mathbf{a}_1) = -l_2 \nabla g(\mathbf{a}_2) \tag{16}$$
$$0 \leq l_1 \perp -f(\mathbf{a}_1) \geq 0 \tag{17}$$
$$0 \leq l_2 \perp -g(\mathbf{a}_2) \geq 0 \tag{18}$$
$$0 \leq \lambda_{in} \perp f(\mathbf{a}_2) \geq 0 \tag{19}$$

Proof. Let us first consider the case when the distance between the objects is greater than zero. In this case $\mathbf{a}_1 \neq \mathbf{a}_2$. Since the gradient vectors cannot be zero and $\hat{l}_1, \hat{l}_2$ in Equation (13), (14) are constrained to be non-negative, $\hat{l}_1, \hat{l}_2$ are strictly positive in this case (from Equations (11) and (12)). Therefore Equation (12) can be written as $\nabla f(\mathbf{a}_1) = -\frac{\hat{l}_2}{\hat{l}_1} \nabla g(\mathbf{a}_2)$. Using $l_1 = \hat{l}_1$ and $l_2 = \frac{\hat{l}_2}{\hat{l}_1}$, Equations (11) to (13) can be written as Equations (15) to (17). Since $\hat{l}_1 > 0$ we can rewrite the complementarity condition in Equation (14) as

$$\begin{aligned} & \hat{l}_2(-g(\mathbf{a}_2)) = 0, \quad \hat{l}_2 \geq 0, \quad -g(\mathbf{a}_2) \geq 0 \\ \Leftrightarrow & \frac{\hat{l}_2}{\hat{l}_1}(-g(\mathbf{a}_2)) = 0 \quad \frac{\hat{l}_2}{\hat{l}_1} \geq 0, \quad -g(\mathbf{a}_2) \geq 0 \\ \Leftrightarrow & l_2(-g(\mathbf{a}_2)) = 0 \quad l_2 \geq 0, \quad -g(\mathbf{a}_2) \geq 0 \end{aligned} \tag{20}$$

Thus Equations (15) to (18) are equivalent to Equations (11) to (14) when the distance between the objects is greater than zero.

When the distance between the objects is equal to zero, we have three facts, namely, (A) $\nabla f(\mathbf{a}_1) \neq 0$, (B) $\nabla g(\mathbf{a}_2) \neq 0$, and (C) $\mathbf{a}_1 = \mathbf{a}_2$. We will first show that $\mathbf{a}_1$ lies on the boundary of F. Using (A) and Equation (15), we have $l_1 = 0$, which implies $f(\mathbf{a}_1) \leq 0$ from Equation (17). However, since $\lambda_{in} > 0$, Equation (19) implies that $f(\mathbf{a}_2) = 0$ and the point $\mathbf{a}_2$ cannot lie within the object defined by function f. Hence, using (C) and $f(\mathbf{a}_1) \leq 0$, we can conclude that $\mathbf{a}_1$ lies on the boundary of object defined by function f. We now show that the point $\mathbf{a}_2$ lies on the boundary of object defined by function g. Equation (16) along with facts (A) and (B) imply that $l_2 > 0$ which in turn implies $g(\mathbf{a}_2) = 0$ from Equation (18). Therefore, $\mathbf{a}_1$ and $\mathbf{a}_2$ lie on the boundaries of the two objects. From Equation (16) and facts (A) and (B) we also see that the normals to the two surfaces are collinear. Thus Equations (15)–(18) together with Equation (19) disallow the interpenetrating case, and we are left with only the touching solution. □

Proposition 2. *Equations* (15) *to* (19) *together represent the contact constraints, i.e., the two objects will satisfy the contact constraints at the end of each time step if and only if Equations* (15) *to* (19) *hold together.*

Proof. As discussed above. □

4.2 Geometrically Implicit Discrete Time Model

We can now rewrite the time-stepping formulation of Equation (6) as a mixed NCP for the geometrically-implicit time-stepper. For each contact k, there is a pair of contact points $\mathbf{a}_{1k}$ and $\mathbf{a}_{2k}$, where the indices 1 and 2 are assigned to the objects arbitrarily as long as they are consistently maintained for a given contact pair. We define vectors $\boldsymbol{\alpha}_1$ and $\boldsymbol{\alpha}_2$ as concatenated vectors of $\mathbf{a}_{1k}$ and $\mathbf{a}_{2k}$ respectively. Thus, the length of $\boldsymbol{\alpha}_1$ and $\boldsymbol{\alpha}_2$ is $3n_c$, where n_c is the number of contacts. For each contact k, we also have the scaled Lagrange multipliers l_{1k} and l_{2k}. We define the vectors $\mathbf{l}_1$ and $\mathbf{l}_2$ as the concatenated vectors of l_{1k} and l_{2k} respectively, and we define $\mathbf{l} = [\mathbf{l}_1; \mathbf{l}_2]$. The vector functions $\mathbf{f}$ and $\mathbf{g}$ are formed by vertical concatenation of the functions defining objects 1 and 2 respectively at each contact. The vector of unknowns, $\mathbf{z}$, can be partitioned into $\mathbf{z} = [\mathbf{u};\ \mathbf{v}]$ where $\mathbf{u} = [\boldsymbol{\nu};\ \boldsymbol{\alpha}_1;\ \boldsymbol{\alpha}_2;\ \mathbf{p}_\mathrm{t};\ \mathbf{p}_\mathrm{o};\ \mathbf{p}_\mathrm{r}]$ and $\mathbf{v} = [\mathbf{l};\ \mathbf{p}_\mathrm{n};\ \boldsymbol{\sigma}]$. Recall that $\boldsymbol{\sigma}$ is the concatenated vector of the magnitude of the slip speed at the contacts. The equality constraints in the mixed NCP are:

$$
\begin{aligned}
0 &= -\mathbf{M}^\ell \boldsymbol{\nu}^{\ell+1} + \mathbf{M}^\ell \boldsymbol{\nu}^\ell + \mathbf{W}_\mathrm{n}^{\ell+1}\mathbf{p}_\mathrm{n}^{\ell+1} + \mathbf{W}_\mathrm{t}^{\ell+1}\mathbf{p}_\mathrm{t}^{\ell+1} + \mathbf{W}_\mathrm{o}^{\ell+1}\mathbf{p}_\mathrm{o}^{\ell+1} + \mathbf{W}_\mathrm{r}^{\ell+1}\mathbf{p}_\mathrm{r}^{\ell+1} + \mathbf{p}_\mathrm{app}^\ell + \mathbf{p}_\mathrm{vp}^\ell \\
\mathbf{q}^{\ell+1} &= \mathbf{q}^\ell + h\mathbf{G}(\mathbf{q}^\ell)\boldsymbol{\nu}^{\ell+1} \\
0 &= (\boldsymbol{\alpha}_1^{\ell+1} - \boldsymbol{\alpha}_2^{\ell+1}) + \mathbf{L}_1 \nabla \mathbf{f}(\boldsymbol{\alpha}_1^{\ell+1}) \\
0 &= \nabla \mathbf{f}(\boldsymbol{\alpha}_1^{\ell+1}) + \mathbf{L}_2 \nabla \mathbf{g}(\boldsymbol{\alpha}_2^{\ell+1}) \\
0 &= \mathbf{E}_\mathrm{t}^2 \mathbf{U}\mathbf{p}_n^{\ell+1} \circ (\mathbf{W}_\mathrm{t}^T)^{\ell+1}\boldsymbol{\nu}^{\ell+1} + \mathbf{p}_\mathrm{t}^{\ell+1} \circ \boldsymbol{\sigma}^{\ell+1} \\
0 &= \mathbf{E}_\mathrm{o}^2 \mathbf{U}\mathbf{p}_n^{\ell+1} \circ (\mathbf{W}_\mathrm{o}^T)^{\ell+1}\boldsymbol{\nu}^{\ell+1} + \mathbf{p}_\mathrm{o}^{\ell+1} \circ \boldsymbol{\sigma}^{\ell+1} \\
0 &= \mathbf{E}_\mathrm{r}^2 \mathbf{U}\mathbf{p}_n^{\ell+1} \circ (\mathbf{W}_\mathrm{r}^T)^{\ell+1}\boldsymbol{\nu}^{\ell+1} + \mathbf{p}_\mathrm{r}^{\ell+1} \circ \boldsymbol{\sigma}^{\ell+1}
\end{aligned}
\tag{21}
$$

where $\mathbf{L}_1$ is a diagonal matrix of size $3n_c \times 3n_c$, with diagonal entries $\mathbf{L}_1(3k-2, 3k-2) = \mathbf{L}_1(3k-1, 3k-1) = \mathbf{L}_1(3k, 3k) = l_{1k}$, $k = 1, \ldots, n_c$, and $\mathbf{L}_2$ is defined similarly to $\mathbf{L}_1$. The complementarity constraints on $\mathbf{v}$ are:

$$
0 \leq \begin{bmatrix} \mathbf{l}_1 \\ \mathbf{l}_2 \\ \mathbf{p}_\mathrm{n}^{\ell+1} \\ \boldsymbol{\sigma}^{\ell+1} \end{bmatrix} \perp \begin{bmatrix} -\mathbf{f}(\boldsymbol{\alpha}_1^{\ell+1}) \\ -\mathbf{g}(\boldsymbol{\alpha}_2^{\ell+1}) \\ \mathbf{f}(\boldsymbol{\alpha}_2^{\ell+1}) \\ \boldsymbol{\zeta} \end{bmatrix} \geq 0 \tag{22}
$$

where $\boldsymbol{\zeta} = \mathbf{U}\mathbf{p}_\mathrm{n}^{\ell+1} \circ \mathbf{U}\mathbf{p}_\mathrm{n}^{\ell+1} - \left(\mathbf{E}_\mathrm{t}^2\right)^{-1}\left(\mathbf{p}_\mathrm{t}^{\ell+1} \circ \mathbf{p}_\mathrm{t}^{\ell+1}\right) - \left(\mathbf{E}_\mathrm{o}^2\right)^{-1}\left(\mathbf{p}_\mathrm{o}^{\ell+1} \circ \mathbf{p}_\mathrm{o}^{\ell+1}\right) - \left(\mathbf{E}_\mathrm{r}^2\right)^{-1}\left(\mathbf{p}_\mathrm{r}^{\ell+1} \circ \mathbf{p}_\mathrm{r}^{\ell+1}\right)$.

In the above formulation, we see $\mathbf{u} \in \mathbb{R}^{6n_b+9n_c}$, $\mathbf{v} \in \mathbb{R}^{4n_c}$, the vector function of equality constraints maps $[\mathbf{u}; \mathbf{v}]$ to $\mathbb{R}^{6n_b+9n_c}$, and the vector function of complementarity constraints maps $[\mathbf{u}; \mathbf{v}]$ to $\mathbb{R}^{4n_c}$ where n_b and n_c are the number of bodies and number of contacts respectively. If using convex bodies only, the upper bound on the number of contacts can be determined directly from the number of bodies, $n_c = \sum_{i=1}^{n_b-1} i$.

4.3 Objects Described by Intersections of Convex Functions

We present here the contact conditions for the general case where each convex object is defined as an intersection of convex inequalities. Let $f_j(\boldsymbol{\xi}_1) \leq 0, j = 1, \ldots, m$, $g_j(\boldsymbol{\xi}_2) \leq 0, j = m+1, \ldots, n$, be $\mathcal{C}^2$ convex functions representing two convex objects (we will call them F and G respectively in the discussion below). Since the closest point is outside the object if it is outside at least one of the intersecting surfaces, the complementarity conditions for nonpenetration can be written as either one of the following two sets of conditions:

$$
\begin{aligned}
&0 \leq \lambda_{in} \perp \max_{j=1,\ldots m} \{f_j(\mathbf{a}_2)\} \geq 0 \\
&0 \leq \lambda_{in} \perp \max_{j=m+1,\ldots n} \{g_j(\mathbf{a}_1)\} \geq 0,
\end{aligned}
\tag{23}
$$

where $\mathbf{a}_1$ and $\mathbf{a}_2$ are the closest points on the two bodies and are given by the KKT conditions

$$\mathbf{a}_1 - \mathbf{a}_2 = -\sum_{i=1}^{m} \hat{l}_i \nabla f_i(\mathbf{a}_1) \tag{24}$$

$$\mathbf{a}_1 - \mathbf{a}_2 = \sum_{j=m+1}^{n} \hat{l}_j \nabla g_j(\mathbf{a}_2) \tag{25}$$

$$0 \leq \hat{l}_i \perp -f_i(\mathbf{a}_1) \geq 0, \quad i = 1, \ldots, m \tag{26}$$

$$0 \leq \hat{l}_j \perp -g_j(\mathbf{a}_2) \geq 0, \quad j = m+1, \ldots, n \tag{27}$$

Analogous to the discussion in Section 4.1, when the distance between the two objects is zero, the KKT conditions in Equations (24)–(27) are valid for common intersection points (i.e., the points may lie within the objects or on the boundaries of the objects). We want to form a system of equations that is equivalent to Equations (24)–(27) when the distance between the objects is non-negative, but only gives the touching solution if the distance is zero.

Note that for objects defined by the intersection of convex functions, there are points on the surface where the normal at the point is not uniquely defined. These points (namely, vertices, and points on edges) lie at the intersection of multiple surfaces, each represented by a convex function. For any point $\mathbf{x}$ that lies at the intersection of multiple surfaces, say $f_i(\mathbf{x}) = 0$, where i belongs to an index set $\mathbb{I}$, we can define a *normal cone*, $\mathcal{C}(F, \mathbf{x})$, that consists of all vectors in the conic hull of the normals to the surfaces. Mathematically,

$$\mathcal{C}(F, \mathbf{x}) = \{\mathbf{y} | \mathbf{y} = \sum_{i \in \mathbb{I}} \beta_i \nabla f_i(\mathbf{x}), \beta_i \geq 0\}.$$

Note that when the index set $\mathbb{I}$ consists of only one surface equation, the normal cone at a point is the half line (with the point as the origin) along the gradient at that point. The normal cone at a point also defines the set of *supporting hyperplanes* to the convex set at that point (Rockafellar, 1970).

We state here, without proof, some basic results from convex geometry that can be deduced from the separating hyperplane theorem for compact sets in finite dimensions (Rockafellar, 1970). The theorem states that two nonempty convex sets in $\mathbb{R}^n$ can be properly separated by a hyperplane if and only if their interiors are disjoint. When the distance between the two objects is strictly positive, the normal to a separating hyperplane is along the line joining the closest points on the two sets. When two objects whose interior are disjoint touch each other, a separating hyperplane is also a supporting hyperplane for both the sets. Thus, in this case, the separating hyperplane theorem implies that *two non-empty convex objects can have a common supporting hyperplane at a point on the boundary of both sets if and only if their interiors are disjoint.* Using the separating hyperplane theorem and the fact that a vector in the normal cone at a point defines a supporting hyperplane, we have the following:

- When the distance between the sets F and G is greater than 0 and $\mathbf{a}_1$ and $\mathbf{a}_2$ are the closest points on the two convex objects, the vector $\mathbf{a}_2 - \mathbf{a}_1$ lies within the set $\mathcal{C}(F, \mathbf{a}_1)$ and also within the set $-\mathcal{C}(G, \mathbf{a}_2)$. Thus, the intersection of the sets $\mathcal{C}(F, \mathbf{a}_1)$ and $-\mathcal{C}(G, \mathbf{a}_2)$ is guaranteed to be non-empty, i.e., $\mathcal{C}(F, \mathbf{a}_1) \cap -\mathcal{C}(G, \mathbf{a}_2) \neq \phi$.
- When the distance between the sets F and G is zero and the two sets are touching at a point $\mathbf{a}_1 = \mathbf{a}_2$ where the normal is not uniquely defined, it is still true that $\mathcal{C}(F, \mathbf{a}_1) \cap -\mathcal{C}(G, \mathbf{a}_2) \neq \phi$.
- However, if the distance is zero, the two points $\mathbf{a}_1 = \mathbf{a}_2$ lie on the boundaries of F and G, and the interiors of the sets F and G intersect, then $\mathcal{C}(F, \mathbf{a}_1) \cap -\mathcal{C}(G, \mathbf{a}_2) = \phi$. This can be seen by noting that in this case there is no supporting hyperplane at $\mathbf{a}_1$ to F (respectively, at $\mathbf{a}_2$ to G) that separates F and G. Since, for a convex set, a vector in the normal cone at a point defines a supporting hyperplane to the set at that point, there is no vector that lies in the normal cone $\mathcal{C}(F, \mathbf{a}_1)$ and also belongs to $-\mathcal{C}(G, \mathbf{a}_2)$.

The three statements above are the formal conditions for the three contact cases shown in Figure 2 that are valid even when the normal at a point on the surface is not unique. In the rest of the paper, we will

abuse terminology and by a normal, we will mean any vector that lies within the normal cone. This will coincide with the actual normal when it is unique. Similarly, by a common normal we will mean any vector in the intersection of $\mathcal{C}(F, \mathbf{a}_1)$ and $-\mathcal{C}(G, \mathbf{a}_2)$.

Proposition 3. *Equations* (28)–(31) *are equivalent to the KKT conditions given by Equations* (24)–(27) *when the distance between the two objects is non-zero. Moreover, when combined with the complementarity condition in Equation* (32)*, we get only the touching solution when the distance between the objects is zero.*

$$\mathbf{a}_1 - \mathbf{a}_2 = -l_{k_1}(\nabla f_{k_1}(\mathbf{a}_1) + \sum_{i=1, i\neq k_1}^{m} l_i \nabla f_i(\mathbf{a}_1)) \tag{28}$$

$$\nabla f_{k_1}(\mathbf{a}_1) + \sum_{i=1, i\neq k_1}^{m} l_i \nabla f_i(\mathbf{a}_1) = -\sum_{j=m+1}^{n} l_j \nabla g_j(\mathbf{a}_2) \tag{29}$$

$$0 \leq l_i \perp -f_i(\mathbf{a}_1) \geq 0 \quad i = 1, \ldots, m \tag{30}$$

$$0 \leq l_j \perp -g_j(\mathbf{a}_2) \geq 0 \quad j = m+1, \ldots, n \tag{31}$$

$$0 \leq \lambda_n \perp \max_{i=1,\ldots,m} \{f_i(\mathbf{a}_2)\} \geq 0 \tag{32}$$

where k_1 is the index of an active constraint on body F and λ_n is the magnitude of the contact force at the contact.

Proof. Let us first consider the case when the distance between the objects is greater than zero, i.e., $\mathbf{a}_1 \neq \mathbf{a}_2$. Since the KKT conditions given by Equations (24)–(27) come from a convex optimization problem, the optimal solution occurs at the boundary of the feasible set and hence there *exists* at least one constraint that is active ((Bazaraa et al., 1993)). This can also be seen from Equation (24) as $\mathbf{a}_1 \neq \mathbf{a}_2$ implies that there is at least one $\hat{l}_i$ that is non-zero (in fact strictly positive, by using Equation 26), i.e, the corresponding constraint is active. Similarly there is at least one $\hat{l}_j, j = m+1, \ldots, n$ that is non-zero. Let $\mathbb{I} = \mathbb{I}_F \cup \mathbb{I}_G$ be the index set of active constraints, where $\mathbb{I}_F$ denotes the set of active constraints for object F and $\mathbb{I}_G$ is the set of active constraints for body G. As stated earlier, $k_1 \in \mathbb{I}$ is the index of an active surface on object F (i.e., the surface on which the closest point lies). Dividing both sides of Equation (25) by $\hat{l}_{k_1}$ and using $l_{k_1} = \hat{l}_{k_1}$, $l_i = \frac{\hat{l}_i}{\hat{l}_{k_1}}, i = 1, \ldots, m, i \neq k_1$, $l_j = \frac{\hat{l}_j}{\hat{l}_{k_1}}, j = m+1, \ldots, n$, we obtain Equations (28) to (29) from Equations (24) to (25) respectively. Equations (30) and (31) can be obtained from Equations (26) and (27) by algebraic manipulation of the complementarity constraints (similar to the one shown in Equation (20)) for all i and j, except $i = k_1$.

Now, let us consider the case when $\mathbf{a}_1 = \mathbf{a}_2$, i.e., the distance between the two objects is zero. We have to show that the Equations (28)–(32) satisfy the following: (a) $\mathbf{a}_1, \mathbf{a}_2$ do not lie within the interior of the two objects and (b) the normal to the two surfaces at $\mathbf{a}_1$ and $\mathbf{a}_2$ respectively, is a common normal. If $\mathbf{a}_2$ lies in the interior of object F, then $f_i(\mathbf{a}_2) < 0, \forall i = 1, \ldots, m$. However this contradicts the right hand part of the complementarity condition given by Equation (32). Thus, $\mathbf{a}_2$ cannot lie within the object F. Since $\mathbf{a}_1 = \mathbf{a}_2$, $\mathbf{a}_1$ has to lie on the boundary of F. Note that $\nabla f_i() \neq 0$ for any point on the boundary of the object F. Now, we want to show by contradiction that $\mathbf{a}_2$ cannot lie within the object G. If $\mathbf{a}_2$ lies within object G, we have $g_j(\mathbf{a}_2) < 0$, and thus from Equation (31), we get $l_j = 0 \ \forall j = m+1, \ldots, n$. This implies that the right hand side of Equation (29) is 0, whereas the left hand side is non-zero, leading to a contradiction. Thus, $\mathbf{a}_2$ lies on the boundary of the object G. Therefore, $\mathbf{a}_1$ and $\mathbf{a}_2$ do not lie in the interior of the two objects and condition (a) above is satisfied.

We will now prove condition (b) above. As stated earlier, by a common normal, here we mean a vector $\mathbf{y} \in \{\mathcal{C}(F, \mathbf{a}_1) \cap -\mathcal{C}(G, \mathbf{a}_2)\}$. Since $\mathbf{a}_1 = \mathbf{a}_2$, and $\nabla f(\mathbf{a}_1)$ is non-zero for all points on the boundary of the set, we have from Equation (28), $l_{k_1} = 0$. Since $\mathbf{a}_1$ lies on the boundary of F, there exists an index set $\mathbb{I}_F$ for which $f_i(\mathbf{a}_1) = 0, i \in \mathbb{I}_F$. We need to consider two cases depending on whether the common normal is uniquely defined or not. We first assume that $\mathbb{I}_F$ consists of only one surface for object F, namely, k_1. In this case, $l_i = 0, i = 1, \ldots, m$. For any solution that satisfies Equation (29), there has to be an index set $\mathbb{I}_G$ with some strictly positive l_j, $j \in \mathbb{I}_G$. This implies that $\nabla f_{k_1}(\mathbf{a}_1) \in -\mathcal{C}(G, \mathbf{a}_2)$ and $\nabla f_{k_1}(\mathbf{a}_1)$ is the common normal. When $\mathbb{I}_F$ consists of more than one surface, the reasoning is analogous as above. Note

that in this case any solution that satisfies Equation (29) can be satisfied by some strictly positive l_i, $i \in \mathbb{I}_F$ and l_j, $j \in \mathbb{I}_G$. This implies that $\mathcal{C}(F, \mathbf{a}_1) \cap -\mathcal{C}(G, \mathbf{a}_2) \neq \phi$ and the left hand side (or right hand side) of Equation (29) gives a common normal. Thus, using the results from convex geometry stated just before the statement of this proposition, we can conclude that the solution of Equations (28) to (31) can only be a touching solution but not an intersecting solution. □

Remark 1. Please note that the correctness of the above proposition requires the existence of an index k_1 in the set of active constraints, which is always the case independent of whether one of the objects is defined by a single surface. For situations where one of the objects is defined only by a single surface, the choice of k_1 can be made beforehand. However, when both objects are described as intersections of surfaces, the choice of k_1 has to be made within a time step and it can vary between time steps. We discuss this in Section 7.

Remark 2. For the proof, we have not made any assumptions about the nature of the surface equations beyond the fact that they be twice continuously differentiable and convex. Thus, the whole framework is also applicable to (a) polyhedral objects (i.e., objects described by intersection of planes), (b) two objects having two different representations (e.g., one polyhedral object and another object described by a nonlinear equation), and (c) a single object having a mixed representation (partly polyhedral and partly with a nonlinear equation).

Proposition 4. *Equations* (28) *to* (32) *together represent the nonpenetration constraints, i.e., the two objects will satisfy the contact constraints at the end of each time step if and only if Equations* (28) *to* (32) *hold together.*

Proof. This claim follows directly from Proposition 3. □

5 Contact Constraints for Quasi-Rigid Bodies

In this section we extend the rigid body contact model of the previous section to quasi-rigid bodies that can be modeled as a rigid core with a thin compliant layer. Our goal is to achieve this without explicit computation of the deformed geometric shape of the objects during contact. We assume that the contact forces and/or moments are produced due to linear deformation and the rate of the deformation, and not due to torsional deflection. Therefore, we use a lumped parameter model of the contact with linear springs and dampers. This assumption models cases where the nominal rigid body contact is a point contact and the point contact deforms to a small area contact. The contact moment is considered only about the normal axis to the contact patch (analogous to soft-finger models in robotic grasping, see (Murray et al., 1994)) and it is assumed that the contact moments about the two axes along the contact patch are negligible.

We now describe the 3D linear viscoelastic model of contact for compliant bodies with a rigid core (which was proposed earlier in (Kraus et al., 1997)) and modify our contact constraints to include the deflections at the contact. We incorporate this model in our time-stepping scheme and present the mixed NCP problem that we are solving at each time step. We extend the Kelvin-Voigt model with the physically motivated observation that the deformations in the normal direction are bounded by some maximum value. For example, a human finger has a thin compliant layer of muscle and tissue surrounding the rigid core (bone). The application of a force on the finger results in a deformation of the thin compliant layer until the rigid core is reached, at which point the non-penetration response is rigid. Therefore, our model allows for a maximum possible deflection, beyond which the contact behaves as a rigid body contact. The linear model can be replaced by a nonlinear model but at the cost of more unknown modeling parameters to be determined experimentally. For each contact i, the normal impact force $\lambda_{i\mathrm{n}}$ is the sum of two components:

$$\lambda_{i\mathrm{n}} = \lambda_{i\mathrm{ns}} + \lambda_{i\mathrm{nr}} \tag{33}$$

where $\lambda_{i\mathrm{ns}}$ is the component of the force that is obtained from the deformation of the spring and damper, and $\lambda_{i\mathrm{nr}}$ is the component from impact with the rigid core. The tangential force at each contact, $\boldsymbol{\lambda}_{i\mathrm{f}} = [\lambda_{i\mathrm{t}}, \lambda_{i\mathrm{o}}]^T$ is also given by a linear spring-damper model. However, we do not have a bound on the maximum displacement in the tangential direction. Concatenating all the individual force components into vectors allows us to write for each contact (we drop subscript i for legibility), $\boldsymbol{\lambda} = \mathbf{K}\boldsymbol{\delta} + \mathbf{C}\dot{\boldsymbol{\delta}}$, where $\boldsymbol{\lambda} = [\lambda_{\mathrm{ns}}, \lambda_{\mathrm{t}}, \lambda_{\mathrm{o}}]^T$ and $\boldsymbol{\delta} = [\delta_{\mathrm{n}}, \delta_{\mathrm{t}}, \delta_{\mathrm{o}}]^T$

are 3×1 column vectors with $\delta_{\rm n}, \delta_{\rm t}, \delta_{\rm o}$ being the normal and tangential deflections respectively. The matrices $\mathbf{K},\ \mathbf{C}$ are stiffness and damping matrices given by

$$\mathbf{K} = \begin{bmatrix} K_{\rm nn} & K_{\rm nt} & K_{\rm no} \\ K_{\rm tn} & K_{\rm tt} & K_{\rm to} \\ K_{\rm on} & K_{\rm ot} & K_{\rm oo} \end{bmatrix} \qquad \mathbf{C} = \begin{bmatrix} C_{\rm nn} & C_{\rm nt} & C_{\rm no} \\ C_{\rm tn} & C_{\rm tt} & C_{\rm to} \\ C_{\rm on} & C_{\rm ot} & C_{\rm oo} \end{bmatrix}$$

For systems with multiple contacts, the contact forces $\boldsymbol{\lambda}$ and body deformations $\boldsymbol{\delta}$ become concatenations of n_c subvectors, where n_c is the number of contacts. The stiffness and damping matrices are block diagonal matrices of size $3n_c \times 3n_c$, where each diagonal block of size 3×3 represents one contact.

5.1 Objects Described by a Single Convex Function

When we consider contact compliance, the contact constraints in Section 4 have to be modified to take into account the deflection of the objects. For our lumped parameter model, we have to compute a point on the two objects where the contact forces due to deformation should be applied. We will refer to this point as the contact point in the remainder of this section. We also have to define a measure of the deflection. Figure 3 is a schematic sketch of two quasi-rigid objects in contact with each other. The bold line schematically illustrates the deformed shapes of the two objects. We define the contact point as the point where the sub-level sets (corresponding to the equations of the objects) shown by dotted lines touch. We define the deflection of an object as the distance between the contact point and a point on the undeformed object along the normal at the contact point. In Figure 3, the deflections for the two objects are denoted by $\delta_{\rm n1}$ and $\delta_{\rm n2}$ respectively. For any quasi-rigid object, we denote the maximum normal deflection by $\delta_{\rm n}^{\rm max} > 0$ and assume that it will be determined experimentally. For simplicity of exposition, we consider only one of the objects to be flexible at the contact. The general formulation where both the bodies are flexible will contain the additional constraint that the contact forces acting on both the bodies have to be equal and opposite. In the following discussion, we will assume $\delta_{\rm n1} = 0$ for simplicity and drop the subscript 2 from $\delta_{\rm n2}$. The constraints for the closest points are given by

$$\begin{aligned} \mathbf{a}_1 - \mathbf{a}_2 &= -l_1 \nabla f(\mathbf{a}_1) \\ \nabla f(\mathbf{a}_1) &= -l_2 \nabla g(\mathbf{a}_2) \\ 0 \le l_1 \perp -f(\mathbf{a}_1) &\ge 0 \\ 0 \le l_2 \perp -(g(\mathbf{a}_2) + \bar{\delta}_{\rm n}) &\ge 0 \end{aligned} \tag{34}$$

where $\bar{\delta}_{\rm n}$ is the *algebraic distance* and $g(\boldsymbol{\xi}_2) + \bar{\delta}_{\rm n} = 0$ is the sub-level set corresponding to the object defined by $g(\boldsymbol{\xi}_2) = 0$. However, the normal contact force is given in terms of the deflection $\delta_{\rm n}$. To obtain the deflection from this algebraic distance we note that the deflection is the distance between the point $\mathbf{a}_2$ and the point where the normal to $g(\boldsymbol{\xi}_2) + \bar{\delta}_{\rm n} = 0$ at $\mathbf{a}_2$ intersects $g(\boldsymbol{\xi}_2) = 0$. From the above argument it can be seen that

$$g\left(\mathbf{a}_2 + \delta_n \frac{\nabla g(\mathbf{a}_2)}{\|\nabla g(\mathbf{a}_2)\|}\right) = 0 \tag{35}$$

The complementarity conditions in Equation (8) thus become:

$$\begin{aligned} 0 \le \lambda_{\rm ns} \perp \psi(\mathbf{a}_1, \mathbf{a}_2) + \bar{\delta}_{\rm n} &\ge 0 \\ 0 \le \lambda_{\rm nr} \perp \delta_{\rm n}^{\rm max} - \delta_{\rm n} &\ge 0 \end{aligned} \tag{36}$$

where $\psi(\mathbf{a}_1, \mathbf{a}_2) = f(\mathbf{a_2})$ or $g(\mathbf{a_1})$ for implicit surfaces.

When the two bodies are not in contact the right hand side of both the complementarity constraints are positive and hence we do not have any contact force. The above equations are to be written for each of the contacting bodies. This formulation ensures that we satisfy the contact constraints at the end of the time step taking into consideration the possibility of the deflection of the body. It does not require the computation of penetration depth for obtaining the deflection as required in (Song et al., 2004a). It ensures that we get a collision response in a fixed time-step scheme.

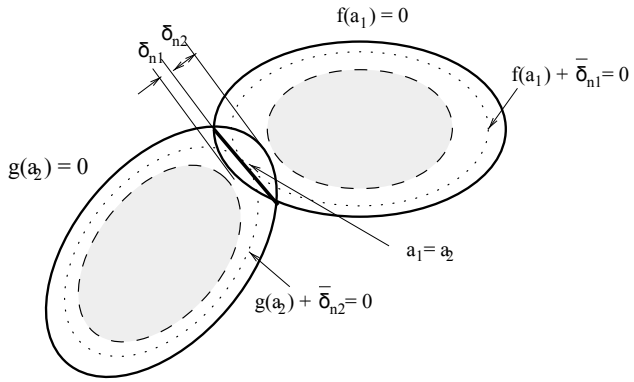

Figure 3: Schematic representation of the deflection at contact. The shaded region is the rigid core of the objects. The contact point is where the dotted curves touch.

We can now formulate the mixed NCP for the geometrically-implicit lumped compliant contact time-stepper. The vector of unknowns $\mathbf{z}$ can be partitioned into $\mathbf{z} = [\mathbf{u};\ \mathbf{v}]$ where

$$\begin{aligned}\mathbf{u} &= [\boldsymbol{\nu};\ \boldsymbol{\alpha}_1;\ \boldsymbol{\alpha}_2;\ \bar{\boldsymbol{\delta}}_{\mathrm{n}};\ \boldsymbol{\delta}_{\mathrm{n}};\ \boldsymbol{\delta}_{\mathrm{t}};\ \boldsymbol{\delta}_{\mathrm{o}};\ \mathbf{p}_{\mathrm{t}};\ \mathbf{p}_{\mathrm{o}};\ \mathbf{p}_{\mathrm{r}}]\\ \mathbf{v} &= [\mathbf{l};\ \mathbf{p}_{\mathrm{ns}};\ \mathbf{p}_{\mathrm{nr}};\ \boldsymbol{\sigma}].\end{aligned}$$

The equality constraints in the mixed NCP are:

$$\begin{aligned}0 &= -\mathbf{M}^{\ell}\boldsymbol{\nu}^{\ell+1} + \mathbf{M}^{\ell}\boldsymbol{\nu}^{\ell} + \mathbf{W}_{\mathrm{n}}^{\ell+1}\mathbf{p}_{\mathrm{n}}^{\ell+1} + \mathbf{W}_{\mathrm{t}}^{\ell+1}\mathbf{p}_{\mathrm{t}}^{\ell+1} + \mathbf{W}_{\mathrm{o}}^{\ell+1}\mathbf{p}_{\mathrm{o}}^{\ell+1} + \mathbf{W}_{\mathrm{r}}^{\ell+1}\mathbf{p}_{\mathrm{r}}^{\ell+1} + \mathbf{p}_{\mathrm{app}}^{\ell} + \mathbf{p}_{\mathrm{vp}}^{\ell}\\ 0 &= \mathbf{p}^{\ell+1} - \left(h\mathbf{K}\boldsymbol{\delta}^{\ell+1} + \mathbf{C}(\boldsymbol{\delta}^{\ell+1} - \boldsymbol{\delta}^{\ell})\right)\\ 0 &= (\boldsymbol{\alpha}_1^{\ell+1} - \boldsymbol{\alpha}_2^{\ell+1}) + \mathbf{L}_1\nabla\mathbf{f}(\boldsymbol{\alpha}_1^{\ell+1})\\ 0 &= \nabla\mathbf{f}(\boldsymbol{\alpha}_1^{\ell+1}) + \mathbf{L}_2\nabla\mathbf{g}(\boldsymbol{\alpha}_2^{\ell+1})\\ 0 &= \mathbf{g}(\boldsymbol{\alpha}_2^{\ell+1} + \mathbf{D}_n^{\ell+1}\frac{\nabla\mathbf{g}(\boldsymbol{\alpha}_2^{\ell+1})}{\|\nabla\mathbf{g}(\boldsymbol{\alpha}_2^{\ell+1})\|})\\ 0 &= \mathbf{E}_{\mathrm{t}}^2\mathbf{U}\mathbf{p}_n^{\ell+1} \circ (\mathbf{W}_{\mathrm{t}}^T)^{\ell+1}\boldsymbol{\nu}^{\ell+1} + \mathbf{p}_{\mathrm{t}}^{\ell+1} \circ \boldsymbol{\sigma}^{\ell+1}\\ 0 &= \mathbf{E}_{\mathrm{o}}^2\mathbf{U}\mathbf{p}_n^{\ell+1} \circ (\mathbf{W}_{\mathrm{o}}^T)^{\ell+1}\boldsymbol{\nu}^{\ell+1} + \mathbf{p}_{\mathrm{o}}^{\ell+1} \circ \boldsymbol{\sigma}^{\ell+1}\\ 0 &= \mathbf{E}_{\mathrm{r}}^2\mathbf{U}\mathbf{p}_n^{\ell+1} \circ (\mathbf{W}_{\mathrm{r}}^T)^{\ell+1}\boldsymbol{\nu}^{\ell+1} + \mathbf{p}_{\mathrm{r}}^{\ell+1} \circ \boldsymbol{\sigma}^{\ell+1}\end{aligned} \tag{37}$$

where $\mathbf{p}^{\ell+1} = [\mathbf{p}_{\mathrm{n}}^{\ell+1};\ \mathbf{p}_{\mathrm{t}}^{\ell+1};\ \mathbf{p}_{\mathrm{o}}^{\ell+1}]$, $\mathbf{p}_{\mathrm{n}}^{\ell+1} = \mathbf{p}_{\mathrm{ns}}^{\ell+1} + \mathbf{p}_{\mathrm{nr}}^{\ell+1}$ and $\boldsymbol{\delta}^{\ell+1} = [\boldsymbol{\delta}_{\mathrm{n}}^{\ell+1};\ \boldsymbol{\delta}_{\mathrm{t}}^{\ell+1};\ \boldsymbol{\delta}_{\mathrm{o}}^{\ell+1}]$. The matrices $\mathbf{L}_1$ and $\mathbf{L}_2$ are as defined in Section 4.2 and $\mathbf{D}_n$ is a $3n_c \times 3n_c$ diagonal matrix with diagonal entries $\mathbf{D}_n(3k-2, 3k-2) = \mathbf{D}_n(3k-1, 3k-1) = \mathbf{D}_n(3k, 3k) = \delta_{nk}$, $k = 1, \ldots, n_c$, with δ_{nk} being the deflection at the kth contact.

The complementarity constraints on $\mathbf{v}$ are:

$$0 \leq \begin{bmatrix}\mathbf{l}_1\\ \mathbf{l}_2\\ \mathbf{p}_{\mathrm{ns}}^{\ell+1}\\ \mathbf{p}_{\mathrm{nr}}^{\ell+1}\\ \boldsymbol{\sigma}^{\ell+1}\end{bmatrix} \perp \begin{bmatrix}-\mathbf{f}(\boldsymbol{\alpha}_1^{\ell+1})\\ -(\mathbf{g}(\boldsymbol{\alpha}_2^{\ell+1}) + \bar{\boldsymbol{\delta}}_{\mathrm{n}}^{\ell+1})\\ \boldsymbol{\psi}(\boldsymbol{\alpha}_1^{\ell+1},\ \boldsymbol{\alpha}_2^{\ell+1}) + \bar{\boldsymbol{\delta}}_{\mathrm{n}}^{\ell+1}\\ \boldsymbol{\delta}_{\mathrm{n}}^{\max} - \boldsymbol{\delta}_{\mathrm{n}}^{\ell+1}\\ \boldsymbol{\zeta}\end{bmatrix} \geq 0 \tag{38}$$

where $\boldsymbol{\zeta} = \mathbf{U}\mathbf{p}_{\mathrm{n}}^{\ell+1} \circ \mathbf{U}\mathbf{p}_{\mathrm{n}}^{\ell+1} - \left(\mathbf{E}_{\mathrm{t}}^2\right)^{-1}\left(\mathbf{p}_{\mathrm{t}}^{\ell+1} \circ \mathbf{p}_{\mathrm{t}}^{\ell+1}\right) - \left(\mathbf{E}_{\mathrm{o}}^2\right)^{-1}\left(\mathbf{p}_{\mathrm{o}}^{\ell+1} \circ \mathbf{p}_{\mathrm{o}}^{\ell+1}\right) - \left(\mathbf{E}_{\mathrm{r}}^2\right)^{-1}\left(\mathbf{p}_{\mathrm{r}}^{\ell+1} \circ \mathbf{p}_{\mathrm{r}}^{\ell+1}\right)$.

In the above formulation, we see $\mathbf{u} \in \mathbb{R}^{6n_b+13n_c}$, $\mathbf{v} \in \mathbb{R}^{5n_c}$, the vector function of equality constraints maps $[\mathbf{u}; \mathbf{v}]$ to $\mathbb{R}^{6n_b+13n_c}$ and the vector function of complementarity constraints maps $[\mathbf{u}; \mathbf{v}]$ to $\mathbb{R}^{5n_c}$ where

n_b and n_c are the number of bodies and number of contacts respectively. If using convex bodies only, the number of contacts can be determined directly from the number of bodies, $n_c = \sum_{i=1}^{n_b} i$. The vector $\boldsymbol{\delta}_{\mathrm{n}}^{\max}$ is the concatenated vector of the maximum deflection of each body (if a body i has n_i contacts, then the corresponding maximum deflection is repeated n_i times in the vector $\boldsymbol{\delta}_{\mathrm{n}}^{\max}$).

5.2 Objects Described by Intersections of Convex Functions

Using the results obtained in Section 4.3 and the previous section, we can now formulate the contact constraints for quasi-rigid bodies where each body is represented as an intersection of convex implicit surfaces. In this case the complementarity conditions for nonpenetration can be written as either one of the following two sets of conditions:

$$\begin{aligned} 0 \leq \lambda_{in} \perp \max_{j=1,\ldots m} \{f_j(\mathbf{a}_2) + \bar{\delta}_{\mathrm{jn}}\} \geq 0 \\ 0 \leq \lambda_{in} \perp \max_{j=m+1,\ldots n} \{g_j(\mathbf{a}_1) + \bar{\delta}_{\mathrm{jn}}\} \geq 0 \end{aligned} \tag{39}$$

Moreover, the closest points on the two objects are given by

$$\begin{aligned} \mathbf{a}_1 - \mathbf{a}_2 &= -l_{k_1}(\nabla f_{k_1}(\mathbf{a}_1) + \sum_{i=1, i\neq k_1}^{m} l_i \nabla f_i(\mathbf{a}_1)) \\ \nabla f_{k_1}(\mathbf{a}_1) + \sum_{i=1, i\neq k_1} l_i \nabla f_i(\mathbf{a}_1) &= -\sum_{j=m+1}^{n} l_j \nabla g_j(\mathbf{a}_2) \\ 0 \leq l_i \perp -f_i(\mathbf{a}_1) &\geq 0 \\ 0 \leq l_j - (g_j(\mathbf{a}_2) + \bar{\delta}_{\mathrm{jn}}) &= 0 \end{aligned} \tag{40}$$

which is a modification of Equations (28) to (31) and the notation is identical to the discussion in Section 4.3. To determine the actual deflection from the algebraic distance, we need to assume that the normal at the point of contact is well defined. Assuming this to be true, we can then obtain the deflection using Equation (35) and the forces on the two bodies can be obtained using the appropriate constitutive laws.

6 Illustrative Examples

In this section we present examples to validate our technique against known analytical results and previous approaches. The first example is for rigid bodies and is the same example of a disc rolling without slip on a plane that we studied in Section 1. The second example consists of a small sphere rolling in contact with two larger spheres, and validates our results against previous simulations of this system. The third example is for quasi-rigid bodies and consists of a unit disc falling on a half-plane with frictionless contact. This example gives a simple validation of our method. The final example is to repeat, in simulation, 100,800 grasping experiments with a parallel jaw gripper conducted by (Brost and Christiansen, 1996).

We use the PATH complementarity solver (Ferris and Munson, 1998) to solve the complementarity problems in this paper. In essence, at each time step, the complementarity system is solved using a Newton-based path following method. In general, there are no theoretical global guarantees of convergence time for Newton-type methods. Therefore, we report the average time taken per iteration for the different problems below for each example. All the examples were implemented in C++ and run times were obtained on a Lenovo T500 laptop with a 2 GHz processor and 2 GB RAM.

6.1 Example 1: Disc on a Plane

In this example we revisit the unit disc example from Section 1. For illustrative purposes, we explain the formulation of the full dynamic model in detail. The normal axis of the contact frame $\hat{\mathbf{n}} = [0, 1]^T$ always points in the inertial y-axis direction and tangential axis $\hat{\mathbf{t}} = [1, 0]^T$ always coincides with the x-direction. The mass matrix, $\mathbf{M}$ is constant and the only force acting on the body is due to gravity. The equation of the

disc is given by $f_1(x,y) = (x-q_x)^2 + (y-q_y)^2 - 1$, where $\mathbf{q} = [q_x, q_y]^T$ is the location of the center of the disc in the inertial frame. Let $\boldsymbol{\nu} = [v_x, v_y, \omega_z]^T$ be the vector of linear and angular velocities and $\mathbf{a}_1$ be the closest point on body 1 (the disc) to the plane (defined by $y = 0$). Similarly, let $\mathbf{a}_2$ be the closest point on the plane to body 1 ($a_{2y} = 0$ and can be removed from the system of unknowns). Thus we have $\mathbf{M} = \text{diag}(m, m, 0.5m)$, where m is the mass of the disc and $0.5m$ the moment of inertia, $\mathbf{p}_{\text{app}} = [0, -mgh, 0]^T$, with $g = 9.81$, the acceleration due to gravity, and

$$\mathbf{r} = \begin{bmatrix} (a_{1x}^{\ell+1} - q_x^{\ell+1}) \\ (a_{1y}^{\ell+1} - q_y^{\ell+1}) \end{bmatrix} \quad \mathbf{W_n} = \begin{bmatrix} \hat{\mathbf{n}} \\ \mathbf{r} \otimes \hat{\mathbf{n}} \end{bmatrix} \quad \mathbf{W_t} = \begin{bmatrix} \hat{\mathbf{t}} \\ \mathbf{r} \otimes \hat{\mathbf{t}} \end{bmatrix} \quad \nabla_{a_1} f_1(a_1^{\ell+1}) = \begin{bmatrix} 2(a_{1x}^{\ell+1} - q_x^{\ell+1}) \\ 2(a_{1y}^{\ell+1} - q_y^{\ell+1}) \end{bmatrix}$$

where $\mathbf{r}$ is the vector from the center of gravity of the disc to $\mathbf{a}_1$ and $\otimes$ connotes the 2D analog of the cross product (for two vectors $\mathbf{x} = [x_1, x_2]^T, \mathbf{y} = [y_1, y_2]^T, x \otimes y = x_1 y_2 - x_2 y_1$). The notation ∇_{a_1} denotes that the gradient is to be computed with respect to the variable $\mathbf{a}_1$.

Assuming that $y = 0$ is the equation of the ground plane, there are 11 unknowns for this system: $\mathbf{z} = [\boldsymbol{\nu};\ \mathbf{a}_1;\ a_{2x};\ l_1;\ l_2;\ p_{\text{n}},;\ p_{\text{t}};\ \sigma]$. The system of equations for the unit disc is:

$$0 = -\mathbf{M}^{\ell}\boldsymbol{\nu}^{\ell+1} + \mathbf{M}^{\ell}\boldsymbol{\nu}^{\ell} + \mathbf{W}_{\text{n}}^{\ell+1} p_{\text{n}}^{\ell+1} + \mathbf{W}_{\text{t}}^{\ell+1} p_{\text{t}}^{\ell+1} + \mathbf{p}_{\text{app}} \tag{41}$$

$$0 = \mathbf{a}_1^{\ell+1} - \mathbf{a}_2^{\ell+1} + l_1 \nabla_{\mathbf{a}_1} f_1(\mathbf{a}_1^{\ell+1}) \tag{42}$$

$$0 = \nabla_{\mathbf{a}_1} f_1(\mathbf{a}_1^{\ell+1}) + l_2 \hat{\mathbf{n}} \tag{43}$$

$$0 = \mu p_{\text{n}}^{\ell+1} (\mathbf{W}_{\text{t}}^{\mathbf{T}^{\ell+1}} \boldsymbol{\nu}^{\ell+1}) + \sigma^{\ell+1} p_{\text{t}}^{\ell+1} \tag{44}$$

$$0 \le l_1 \perp f_1(\mathbf{a}_1^{\ell+1}) \ge 0 \tag{45}$$

$$0 \le p_n^{\ell+1} \perp f_1(\mathbf{a}_2^{\ell+1}) \ge 0 \tag{46}$$

$$0 \le \sigma \perp \mu^2 p_{\text{n}}^{\ell+1} p_{\text{n}}^{\ell+1} - p_{\text{t}}^{\ell+1} p_{\text{t}}^{\ell+1} \ge 0 \tag{47}$$

Equation (44) can be obtained from Equation (21) by noting that for a $2D$ problem, $\mathbf{p}_o = \mathbf{p}_r = 0$. Furthermore, in this case $E_t = 1$, $\mathbf{U} = \mu$ and the Hadamard product is equivalent to scalar multiplication. Similar reasoning also gives Equation (47) from the last complementarity constraint in Equation (22).

The initial configuration of the disc is $\mathbf{q} = [0, 1, 0]^T$, initial velocity is $\boldsymbol{\nu} = [-3, 0, 3]^T$, mass is $m = 1$, and $\mu = 0.4$. Figure 1a shows the kinetic energy of the disc for our implicit representation along with the Stewart-Trinkle LCP implementation using various levels of discretization as it rolls along the horizontal surface. When using an implicit curve representation to model the disc and our new formulation presented above, we get no energy loss (within the numerical tolerance of 10^{-6} used for our simulations) as seen by the horizontal line. The time step used was 0.01 seconds and the average time taken for simulating each time step was 0.02 seconds. When using the LCP formulation, we have energy loss as discussed earlier.

6.2 Example 2: Sphere on Two Spheres

This example consists of a small sphere moving in contact with two larger fixed spheres. This example is chosen to compare the results of our geometrically-implicit method to those presented in (Trinkle et al., 2001) and (Liu and Wang, 2005) ((Trinkle et al., 2001) was able to solve this problem with implicit geometric information because a closed form distance function is available between two spheres). Figure 4a shows a small unit sphere in simultaneous contact with two larger fixed spheres. The sphere of radius 10 units is located at (0, 0, 0) in the inertial frame and the sphere of radius 9 units is located at (0, 11.4, 0). The contact of the small sphere with the largest sphere (on the right) is labeled Contact 1 and the contact with the sphere on the left is labeled Contact 2. There is also a constant force of $\lambda_{app} = [1.0,\ 2.6,\ -9.81,\ 0,\ 0,\ 0]^T$ applied to the small sphere. With this force, the sphere initially has one of its contacts (Contact 1) rolling while the other contact (Contact 2) is simultaneously sliding, the rolling contact transitions to sliding, and both contacts eventually separate. It is important to emphasize that all these transitions are captured using a fixed time step implementation.

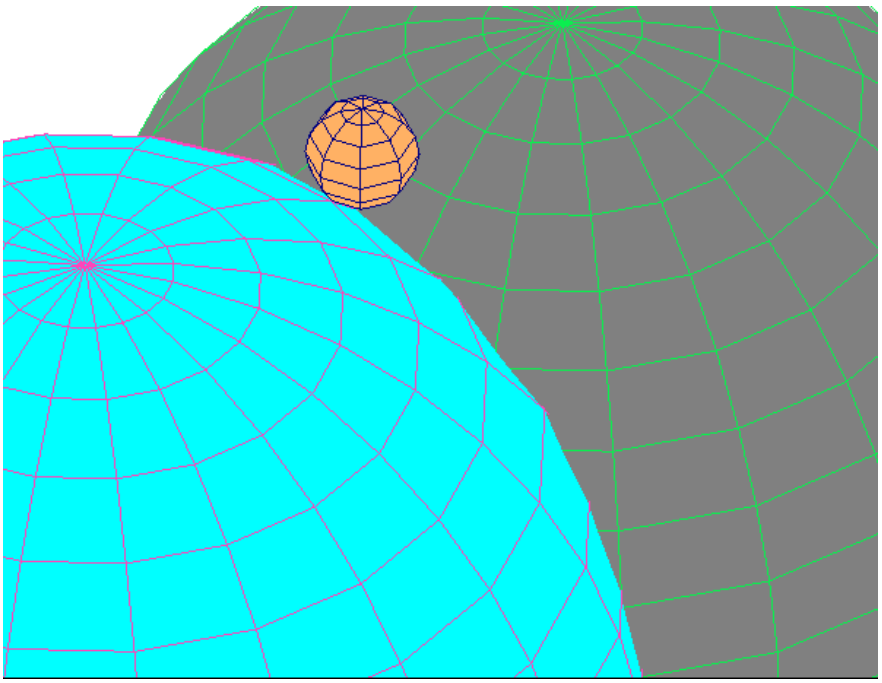

(a) A small sphere in contact with two large spheres.

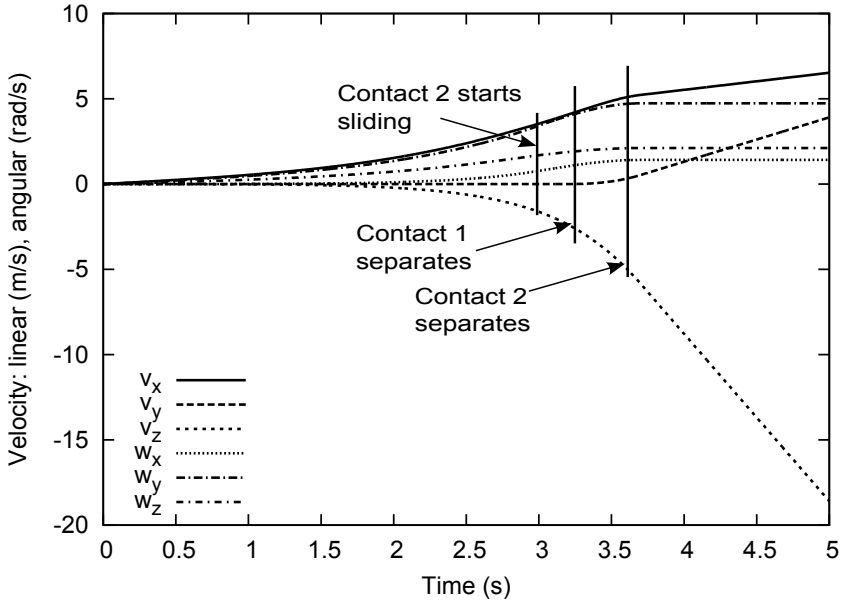

(b) Velocities of small moving sphere.

Figure 4: Example of a sphere on two spheres, illustrating contact transitions.

The initial configuration and velocity of the small moving sphere is

$$\mathbf{q} = [0,\ 6.62105263157895,\ 8.78417110772903,\ 1,\ 0,\ 0,\ 0]^T$$
$$\boldsymbol{\nu} = [0,\ 0,\ 0,\ 0,\ 0,\ 0,\ 0]^T.$$

The friction parameters are: $e_t = 1$, $e_o = 1$, $e_r = 0.3$, and $\mu = 0.2$. There are 32 variables in our NCP formulation (6 velocity variables and 13 variables for each contact: 6 contact point coordinates for the two bodies, 2 Lagrange multipliers, 4 contact impulses and σ for the contact). We used a step size $h = 0.01$ (Tzitzouris-Pang use $h = 0.1$). The running time for each time step is 0.4 seconds when the small sphere is in contact with both the spheres and 0.05 seconds when the small sphere is in free fall (note that the size of the problem was not changed during free fall, there were 32 variables and 32 nonlinear equations and complementarity constraints).

The generalized velocity of the sphere is shown in Figure 4b. The smooth velocity profile agrees well with the nonlinear Tzitzouris-Pang formulation (Trinkle et al., 2001). The Liu-Wang formulation (Liu and Wang, 2005) experienced non-smooth velocity jumps when the small sphere separated from the larger fixed spheres, which they attributed to an explicit time-stepping scheme. In the LCP Stewart-Trinkle implementation, the velocity profiles and the force profiles were very non-smooth (please see Figures 10 and 11 of (Trinkle et al., 2001)). These results further confirm our belief that both linearization and explicit time-stepping lead to inaccuracies.

The fidelity of our method is further emphasized by Figures 5a and 5b that show the forces and sliding speed magnitudes at the two contacts. Contact 1 starts as a sliding contact and we see the sliding speed increases as the normal force decreases. Also, the magnitude of the friction force is equal to $\mu\lambda_{1n}$, consistent with our friction law for a sliding contact. At approximately 3.2 seconds, the small sphere separates from the large sphere at this contact, and all forces acting at contact 1 and the sliding speed drop to zero. Contact 2 on the other hand starts out as a rolling contact until approximately $t = 3$ seconds when it transitions to sliding. During the rolling phase the frictional magnitude is bounded by $\mu\lambda_{2n}$ as required by the friction law, and the sliding speed is 0. At the transition to sliding, the magnitude of the friction force becomes equal to $\mu\lambda_{2n}$ and the sliding speed begins to increase. Finally, at approximately $t = 3.6$ seconds, the contact breaks and all forces at this contact and the sliding speed drop to zero.

6.3 Example 3: Disc Falling on a Quasi-Rigid Half-Plane

In this example, we simulate a rigid unit disc falling onto a quasi-rigid horizontal half-plane. The contact is modeled as a single frictionless contact with no damping. Depending on the value of maximum deflection, the disc may or may not make contact with the rigid core of the half-plane. Figure 6 illustrates the problem.

There are 12 unknowns in this system, with 4 complementarity constraints:

$$\mathbf{z} = [\mathbf{u}; \mathbf{v}] = [v_x, v_y, \omega, a_{1x}, a_{1y}, a_{2x}, a_{2y}, l_1, l_2, \delta_n, p_{\rm ns}, p_{\rm nr}]^T.$$

The equations of motion for this system are (omitted superscripts indicate time ℓ, except for the Lagrange multipliers l_1 and l_2 that are always evaluated at $\ell + 1$):

$$0 = -\mathbf{M}^\ell \boldsymbol{\nu}^{\ell+1} + \mathbf{M}^\ell \boldsymbol{\nu}^\ell + \mathbf{W}_{\rm n}^{\ell+1} p_{\rm ns}^{\ell+1} + \mathbf{W}_{\rm n}^{\ell+1} p_{\rm nr}^{\ell+1} + \mathbf{p}_{\rm app} \tag{48}$$
$$0 = p_{\rm ns}^{\ell+1} - hk\delta_n^{\ell+1} \tag{49}$$
$$0 = \mathbf{a}_2^{\ell+1} - \mathbf{a}_1^{\ell+1} + l_1\hat{\mathbf{n}} \tag{50}$$
$$0 = l_2 \nabla_{\mathbf{a}_1} f_1(\mathbf{a}_1^{\ell+1}) + \hat{\mathbf{n}} \tag{51}$$
$$0 \le l_2 \perp f_1(\mathbf{a}_1^{\ell+1}) \ge 0 \tag{52}$$
$$0 \le l_1 \perp a_{2y}^{\ell+1} + \delta_{\rm n}^{\ell+1} \ge 0 \tag{53}$$
$$0 \le p_{\rm ns}^{\ell+1} \perp a_{1y}^{\ell+1} + \delta_{\rm n}^{\ell+1} \ge 0 \tag{54}$$
$$0 \le p_{\rm nr}^{\ell+1} \perp \delta_{\rm n}^{o} - \delta_{\rm n}^{\ell+1} \ge 0 \tag{55}$$

The unit disc's initial position was $\mathbf{q} = [0,\ 1.5, 0]^T$ with zero initial velocity $\boldsymbol{\nu} = [0,\ 0,\ 0]^T$. The only force acting on the disc was gravity. The mass of the disc was 1 kg and the moment of inertia about the

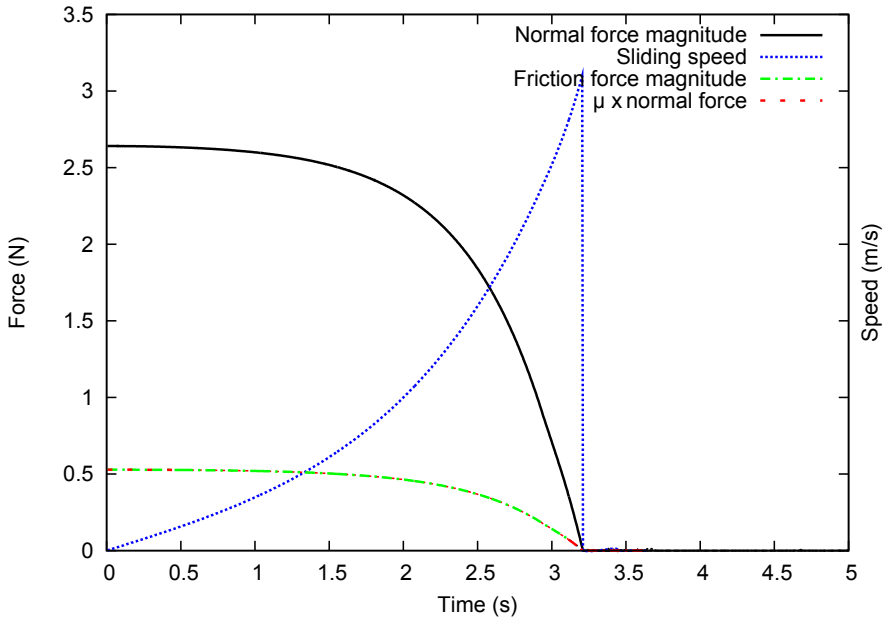

(a) Force and sliding speed at contact 1.

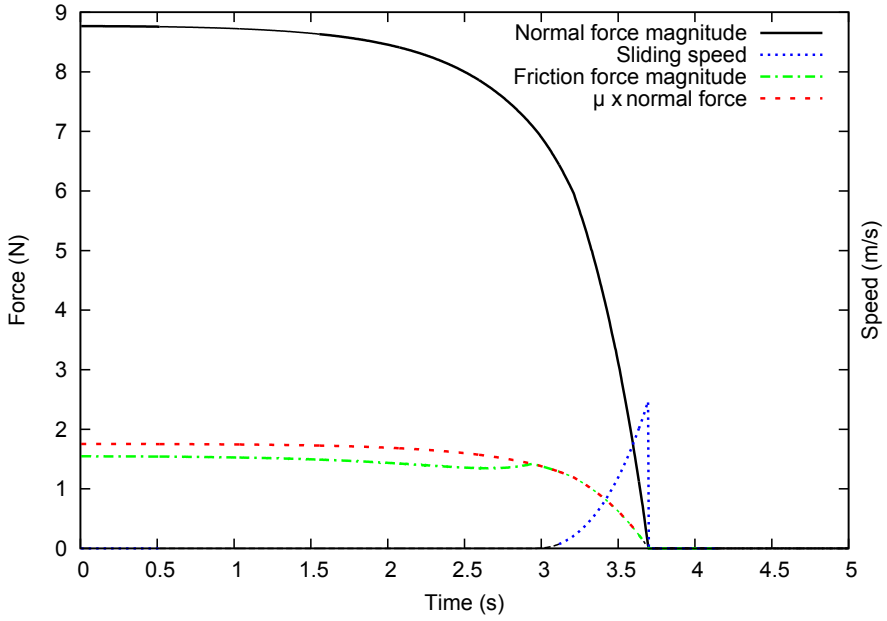

(b) Force and sliding speed at contact 2.

Figure 5: Contact 1 is always sliding until separation, hence the curve of $\mu \times$ normal force (at contact 1) and the friction force magnitude curve overlap for the duration. Contact 2 is a rolling contact until 3 seconds, whence it transitions to a sliding contact, hence the curve of $\mu \times$ normal force (at contact 1) lies below the friction force magnitude curve up to 3 seconds, and the two curves overlap thereafter. The contact forces become 0 when contact is lost (at approximately 3.2 seconds for contact 1 and 3.6 seconds for contact 2). The value of μ is 0.2.

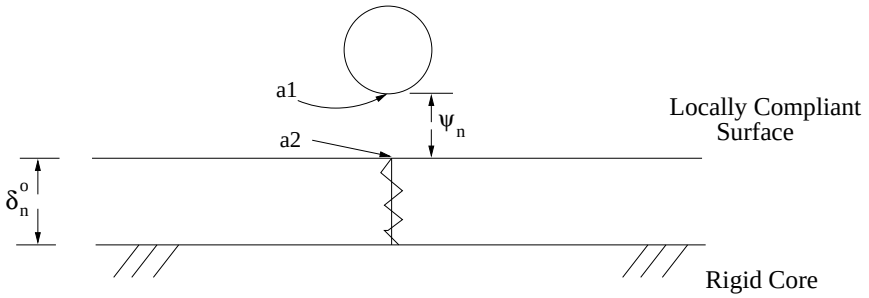

Figure 6: Unit disc falling onto a frictionless quasi-rigid surface.

center of mass was 0.5 kg· m^2. We used a step size $h = 10^{-4}$s. The spring stiffness we used was $k = 1000$ kg/s^2. The maximum penetration depth was altered for two experiments such that for the first experiment impact with the rigid core occurs, and for the second experiment impact with the rigid core does not occur. For the first experiment, $\delta_n^{\max}$ is 0.05m and for the second experiment $\delta_n^{\max}$ is 1m.

Figure 7 illustrates the results of the first experiment in which the maximum spring deflection was not large enough to prevent impact with the rigid core. There is a large non-penetration impulse (see Figure 7a) generated at approximately 0.34 seconds corresponding to when the spring reached maximum deflection and impact with the rigid core occurs. As expected with a rigid impact, we also see an instantaneous change in velocity to zero (see Figure 7d) and loss of energy (see Figure 7e). After the impact, the motion of the disc becomes oscillatory (see Figure 7c) as it bounces on the undamped spring (see Figure 7b, which clearly shows the oscillatory nature of the spring force). Furthermore, the velocity of the disc is smooth (see Figure 7d). As seen in Figure 7e the total energy is preserved after impact within a tolerance of 10^{-5}J, which is acceptable using a time step of 10^{-4}s and an Euler approximation in the time-stepping formulation. The average time taken for each iteration is 0.03 seconds.

For the second experiment, the maximum spring deflection was set large enough that impact with the rigid core never occurs. We see the oscillatory behavior of the position over the lifetime of the simulation (Figure 8c) as expected with an undamped spring. As guaranteed by our model, no component of the normal force comes from impact with the rigid core; the spring contributes solely to the normal force (Figure 8b). Additionally, without any impacts the plot of velocity is smooth with changes occurring only from the force of gravity and the spring force (Figure 8d). Since there is no impact nor damping of the spring, we expect there to be no loss of energy in the system. Figure 8a confirms this, where again the energy is conserved within a numerical tolerance of 10^{-5}J.

6.4 Example 4: Probabilistic Grasp Planning

We repeated, in simulation, an earlier grasping experiment conducted by (Brost and Christiansen, 1996). The experiment was designed to study the probability of success of a particular strategy for achieving a stable grasp of the lock piece (about 21 mm in diameter) shown in Figure 9. The strategy was to place a parallel-jawed gripper around the piece and close the grippers (symmetrically) until closing was stopped. Upon stopping, if the part was held by its outer-most teeth, the grasp strategy was declared successful. All other outcomes were considered failures. The goal of the experiment was to find the initial location (x, y) (shown in Figure 9) for the center of the fingertips with the greatest probability of success (given some positioning error).

At Sandia National Laboratories 100,800 grasp trials were conducted over a period of weeks, with considerable technician support and dedicated robotics equipment. Figure 10a shows half of a symmetric histogram constructed from the trials. For many different values of (x, y), a grasp was attempted. The height of the histogram over each square millimeter patch in the (x, y)-plane is the fraction of successful trials out of all trials with initial conditions in that patch. Note that the "sweet spot" is at about $(0, -11)$mm. Squeezing from this position causes contact with the circular portion of the perimeter far enough below the center to cause the piece to slide upward as the jaws close - ultimately coming to rest on the outer-most teeth. Even if the robot's positioning error was roughly $\pm$3mm in the x- and y-directions away from the sweet spot, the

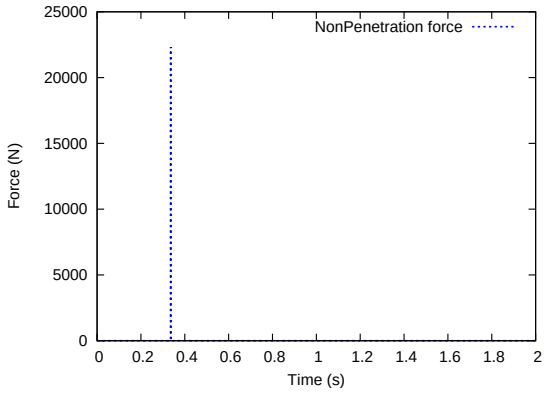

(a) Non-penetration force is non-zero when the disc contacts the rigid core.

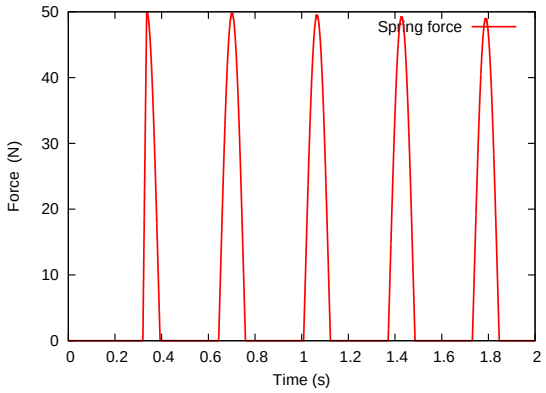

(b) Spring force is non-zero when the disc is in contact with the plane.

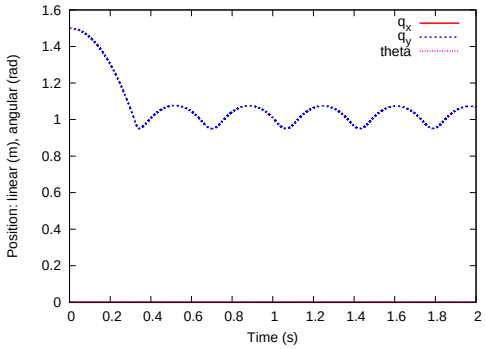

(c) Position of the disc's center. Note that q_x and θ remain zero throughout, so they cannot be distinguished in the plot.

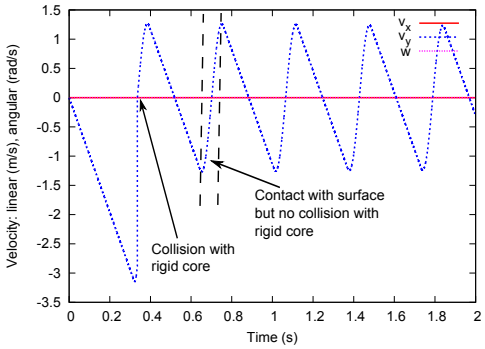

(d) Velocity of the disc. Note that the linear velocity, v_x, and the angular velocity, ω, are zero throughout, so the two curves overlap. For clarity, one region of motion with contact with the surface but no contact with rigid core is demarcated by dashed vertical lines.

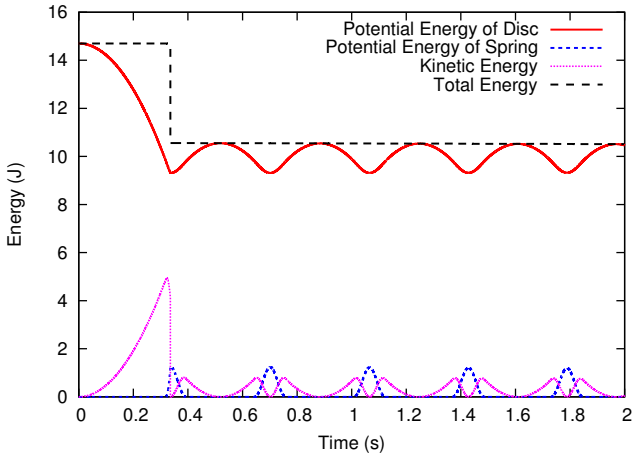

(e) Variation of energy with time. Note that the drop in total energy is due to collision with the rigid core, and that energy is conserved when there is no collision with rigid core.

Figure 7: Simulation results for a unit disc falling on a half-plane making contact with the rigid core.

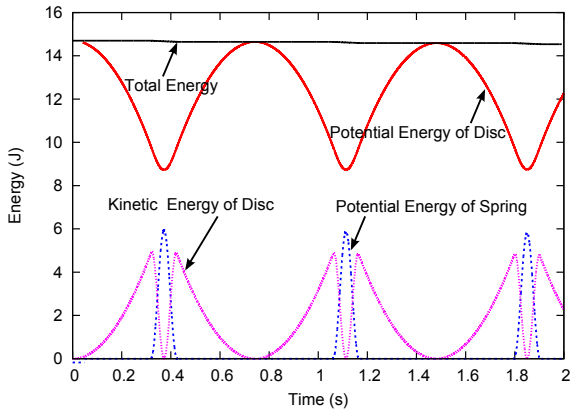

(a) Energy

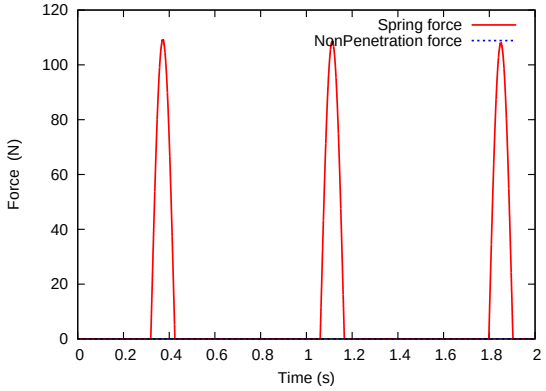

(b) Force plot. The non-penetration force is zero in this case since there is no contact with the rigid core.

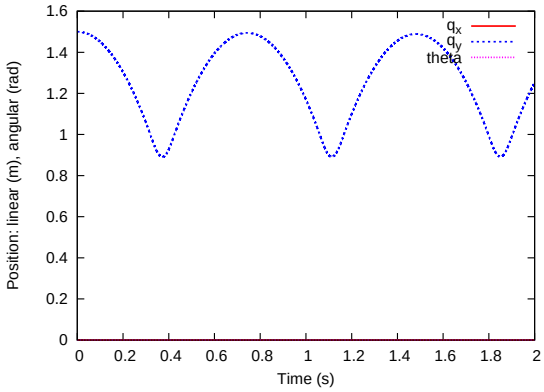

(c) Position plot. Note that q_x and θ remain zero throughout, so they cannot be distinguished in the plot.

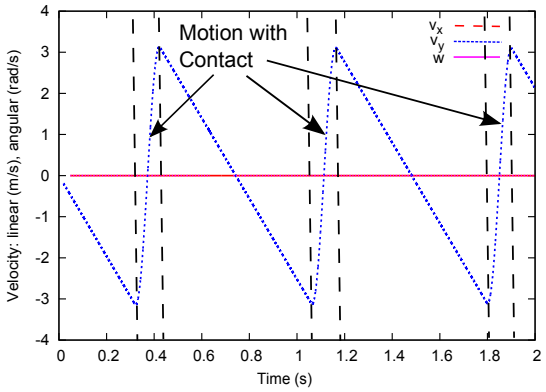

(d) Velocity plot showing the regions of motion in contact with the surface (demarcated by dashed vertical lines). Note that here also the linear velocity v_x along the x-axis and the angular velocity ω are zero. Hence they cannot be distinguished in the plot.

Figure 8: Simulation results for a unit disc falling on a half-plane without making contact with the rigid core.

probability of success is very high.

The goal of our simulation study was to learn if the sweet spot could be found through simulation in dVC, which is cheaper and faster than experimental trials in the lab. To conduct our study, we modeled the gear as a union of superellipses (Barr, 1981) and modeled the grippers as intersections of half-planes. Let $\mathbf{q} = [x_g,\ y_g,\ \theta_g,\ x_r,\ x_l]^T$ be the generalized configuration of the system, where $[x_g,\ y_g,\ \theta_g]^T$ is the position and orientation of the gear, x_r is the x-position of the right gripper's fingertip, and x_l is the x-position of the left gripper's fingertip.

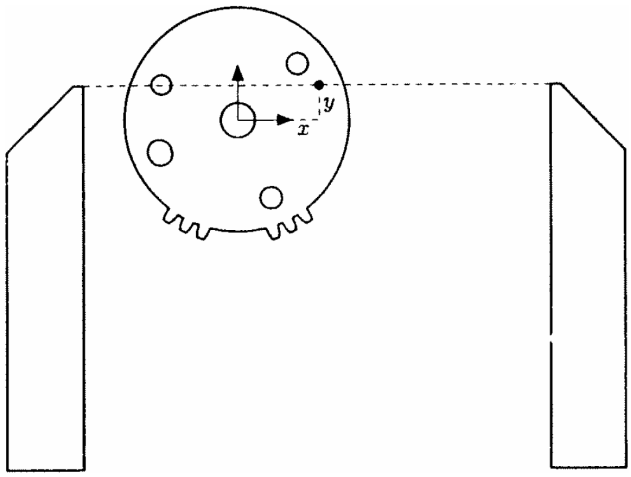

Figure 9: The parameterization of the parallel jaw gripper and gear system as shown in (Brost and Christiansen, 1996).

The gear's equations are given by the union of:

$$f(\xi_x, \xi_y) \equiv (\xi_x - q_1)^2 + (\xi_y - q_2)^2 - 20.75 = 0 \tag{56}$$

$$f_i(\xi_x, \xi_y) \equiv \left(\frac{\xi_x - (q_1 + r_{ix})}{2.3}\right)^4 + \left(\frac{\xi_y - (q_2 + r_{iy})}{1.1}\right)^4 - 1 = 0 \tag{57}$$

where q_i is the ith component of $\mathbf{q}$ and $\mathbf{r}_i$ is the vector from the gear's center of mass to the center of the ith tooth[1]. The values used for this simulation were $\mathbf{r}_i = 20.75[\cos(\theta_i),\ \sin(\theta_i)]^T$, where $\theta_1 = 4.103727$ rads, $\theta_2 = 4.253125$ rads, $\theta_3 = 4.402522$ rads, $\theta_4 = 5.022255$ rads, $\theta_5 = 5.171653$ rads, and $\theta_6 = 5.321051$ rads.

During each simulation, the grippers only make contact with the gear with their respective fingertip vertex, inside edge, or top edge. Therefore we simplify the modeling of the grippers to be the intersection of the two planes adjacent to the fingertip vertex. For the right gripper, the equations are given by the intersection of:

$$f_{r1}(\xi_x, \xi_y) \equiv \xi_y = 0 \tag{58}$$

$$f_{r2}(\xi_x, \xi_y) \equiv -(\xi_x - q_4) = 0 \tag{59}$$

and for the left gripper, the equations are given by the intersection of:

$$f_{l1}(\xi_x, \xi_y) \equiv \xi_y = 0 \tag{60}$$

$$f_{l2}(\xi_x, \xi_y) \equiv \xi_x - q_5 = 0 \tag{61}$$

[1]For brevity, frame transformations have not been shown; in practice one must be careful to maintain frame consistency.

The non-penetration constraint between the right gripper and the disc part of the gear is:

$$0 = \mathbf{a}_2 - \mathbf{a}_1 + l_1 \nabla_{\mathbf{a}_2} f(\mathbf{a}_2) \tag{62}$$
$$0 = \nabla_{\mathbf{a}_2} f(\mathbf{a}_2) + l_2 \nabla_{\mathbf{a}_1} f_{r1}(\mathbf{a}_1) + l_3 \nabla_{\mathbf{a}_1} f_{r2}(\mathbf{a}_1) \tag{63}$$
$$0 \leq l_1 \perp -f(\mathbf{a}_2) \geq 0 \tag{64}$$
$$0 \leq l_2 \perp -f_{r1}(\mathbf{a}_1) \geq 0 \tag{65}$$
$$0 \leq l_3 \perp -f_{r2}(\mathbf{a}_1) \geq 0 \tag{66}$$
$$0 \leq \lambda_{in} \perp f(\mathbf{a}_1) \geq 0 \tag{67}$$

where $\mathbf{a}_1$ is the closest point on the right gripper to the disc, $\mathbf{a}_2$ is the closest point on the disc to the right gripper, and λ_{in} is the component of the non-penetration force associated with this contact. The remaining contact constraints can be formulated analogously.

Friction in the plane of motion is important, so for this problem we used a 2.5D dynamic model (Berard et al., 2007), with force-controlled parallel jaw grippers. In order to simulate the original experiments, we assumed that the coefficient of surface friction and coefficient of gripper friction were unknown parameters, but bounded. Then for each (x_i, y_i) in a 20mm by 20mm box of initial positions (sampled at 1mm resolution), we assigned random values to the unknown parameters and simulated the grasping strategy. The success probability for each (x_i, y_i) pair was estimated as the total number of successful grasps divided by the number of trials.

Figure 10 illustrates a comparison between our results and those reported by Brost and Christiansen. Let us refer to the large contiguous region where the probability of success is nearly one, as the "plateau." Note that the shapes of the plateaus are quite similar. Two quantitative differences are the slopes of the drop-offs and the size of low areas for values of small y (on the back sides of the plateaus). The difference in the sharpness of the drop-offs is most likely due to our bounds on the coefficients of friction. We have no way of recovering effective friction coefficients from the experiments, but we conjecture that they varied more widely than they did in our simulated experiments. The low areas behind the plateaus correspond to initial positions of the gripper such that closing will achieve a grasp of nearly diametrically opposite points on the lock piece. The width of the low area turns out to be a complex function of the details of the controller of the gripper and the coefficients of friction between the lock piece and the support and the lock piece and the gripper. Overall, the comparison is quite good. As one can see, the size and shape of the sweet spot found via simulation is nearly identical to that found experimentally.

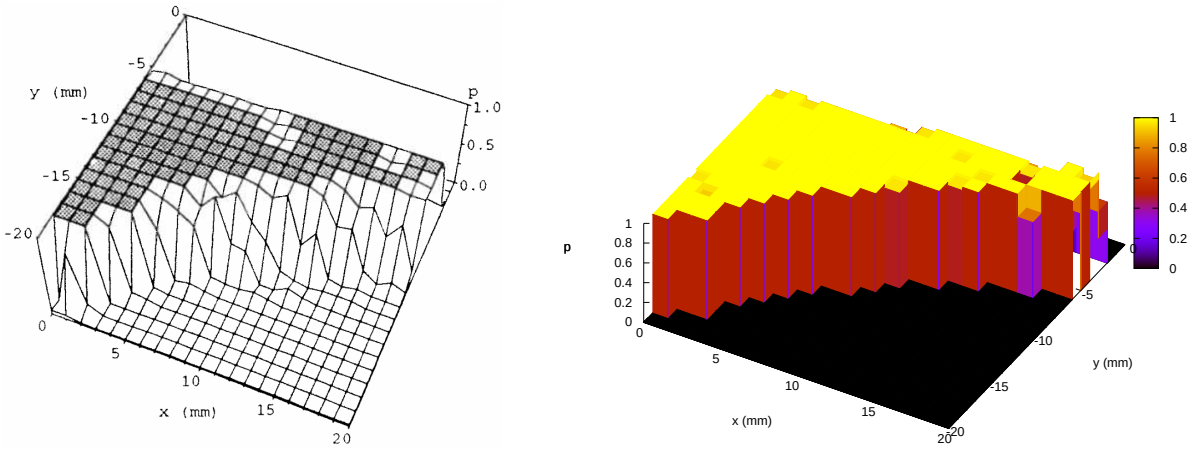

(a) Actual (b) Simulation

Figure 10: Comparison of (a) the experimental results of Brost and Christiansen (reproduced from (Brost and Christiansen, 1996)) to (b) our simulation results.

7 Discussion on Implementation Issues

Although the theoretical formulation in this paper is valid for objects described as an intersection of convex $\mathcal{C}^2$ functions, for implementation with existing MNCP complementarity solvers, we need to restrict ourselves to cases where one object is described by a single equation. In all of the examples above, we have used the PATH solver (Ferris and Munson, 1998) to solve the complementarity problem at each time step. PATH relies on a Newton-based method with path search (instead of line search) for iteratively solving the system of equations at each time step (Dirkse and Ferris, 1995; Ralph, 1994). When any one of the objects is defined by a single equation, this constraint is always active, i.e., k_1 in Equation 29 is known a priori. Therefore, we can use the Equations (28) to (31) along with the discretized equations of motion and complementarity constraints coming from contact and friction to form the system of equations and inequalities that are to be input to PATH. However, when both objects are described by intersections of convex functions, the active constraint on which the closest point lies will vary with time. So, we cannot identify an index k_1 a priori to write Equation (29) in the given form.

In principle, this problem can be mitigated by using recently proposed active set methods for solving the mixed nonlinear complementarity problem (MNCP) (Izmailov and Solodov, 2008). Active set methods also use a Newton-based method for solving the MNCP. However, they do not use all the equations while solving the MNCP. The key idea here is to iteratively identify a set of potential active constraints and formulate and solve a smaller system of equations by removing the inactive constraints. The smaller set of equation can be potentially solved faster, however, multiple systems of nonlinear equations have to be solved for different guesses of the active set. This is especially true when there are a large number of constraints that can be inactive in the optimal solution or when we are repeatedly solving a collection of equations whose coefficients change with time (as is the case in dynamic simulation). The identification of the active set can be done in a principled way as outlined in (Facchinei et al., 1998). However, we are not aware of any publicly available implementations of this scheme. A robust implementation of this scheme is a research problem by itself and is beyond the scope of this paper.

8 Conclusion

We presented the first geometrically implicit time-stepping scheme for dynamic simulation of objects described as intersections of convex inequalities. This approach overcomes stability and accuracy problems associated with polygonal approximations of smooth objects and approximation of the distance function for two objects in intermittent contact. We developed a new formulation for the contact constraints in the work space which enabled us to formulate a geometrically implicit time-stepping scheme as a nonlinear complementarity problem. We demonstrated through example simulations the fidelity of this approach to analytical solutions, previously described simulation results, and physical experiments. This method can provide a baseline for understanding and quantifying the errors incurred when using a geometrically explicit method and when making various linearizing approximations. In the future we wish to conduct such studies. Our ultimate future goal is to develop techniques for automatically selecting the appropriate method for a given application, and to guide method switching, step size adjustment, and model approximations in real time.

Acknowledgment

We wish to thank Todd Munson for his insightful discussions on NCPs. We thank the anonymous reviewers for their detailed comments and constructive suggestions. This work was supported by the National Science Foundation under grants IIS-0093233(CAREER), 0139701 (DMS-FRG), 0413227 (IIS-RCV), 0420703 (MRI), CCF-0729161, and CCF-1048261.

References

Anitescu, M., Cremer, J. F., and Potra, F. A. (1996). Formulating 3D contact dynamics problems. *Mechanics of Structures and Machines*, 24(4):405.

Baraff, D. (1990). Curved surfaces and coherence for non-penetrating rigid body simulation. *Computer Graphics*, 24(4):19–28.

Barr, A. H. (1981). Superquadrics and angle-preserving transformations. *IEEE Computer Graphics and Applications*, 1(1):11–23.

Bazaraa, M. S., Sherali, H. D., and Shetty, C. M. (1993). *Nonlinear Programming: Theory and Algorithms*. John Wiley, New York, second edition.

Berard, S., Egan, K., and Trinkle, J. C. (2004). Contact modes and complementary cones. In *IEEE International Conference on Robotics and Automation*, New Orleans, LA.

Berard, S., Nguyen, B., Trinkle, J. C., and Anderson, K. (2010). Sources of error in a simulation of rigid parts on a vibrating rigid plate. *Journal of Computational Nonlinear Dynamics*, 5(4).

Berard, S., Trinkle, J., Nguyen, B., Roghani, B., Kumar, V., and Fink, J. (2007). daVinci code: A multi-model simulation and analysis tool for multi-body systems. In *IEEE International Conference on Robotics and Automation*, pages 2588–2593, Rome, Italy.

Brost, R. C. and Christiansen, A. D. (1996). Probabilistic Analysis of Manipulation Tasks: A Conceptual Framework. *The International Journal of Robotics Research*, 15(1):1–23.

Chakraborty, N., Berard, S., Akella, S., and Trinkle, J. C. (2007a). An implicit time-stepping method for multibody systems with intermittent contact. In *Robotics: Science and Systems Conference*, pages 177–184, Atlanta, GA.

Chakraborty, N., Berard, S., Akella, S., and Trinkle, J. C. (2007b). An implicit time-stepping method for quasi-rigid multibody systems with intermittent contact. In *Proceedings of ASME IDETC 2007*, Las Vegas, NV. DETC2007-35526.

Chakraborty, N., Peng, J., Akella, S., and Mitchell, J. E. (2008). Proximity queries between convex objects: An interior point approach for implicit surfaces. *IEEE Transactions on Robotics*, 24(1):211–220.

Cherif, M. and Gupta, K. K. (1999). Planning quasi-static fingertip manipulation for reconfiguring objects. *IEEE Transactions on Robotics and Automation*, 15(5):837–848.

Cottle, R. W., Pang, J. S., and Stone, R. E. (1992). *The Linear Complementarity Problem*. Academic Press.

Dirkse, S. P. and Ferris, M. C. (1995). The PATH solver: A non-monotone stabilization scheme for mixed complementarity problems. *Optimization Methods and Software*, 5:123–156.

Egan, K. T., Berard, S., and Trinkle, J. C. (2003). Modeling nonconvex constraints using linear complementarity. Technical Report 03-13, Department of Computer Science, Rensselaer Polytechnic Institute.

Facchinei, F., Fischer, A., and Kanzow, C. (1998). On the accurate identification of active constraints. *SIAM Journal on Optimization*, 9(1):14–32.

Ferris, M. C. and Munson, T. S. (1998). Complementarity problems in GAMS and the PATH solver. Technical Report MP-TR-1998-12, Department of Computer Science, University of Wisconsin, Madison.

Gilardi, G. and Sharif, I. (2002). Literature survey of contact dynamics modeling. *Mechanism and Machine Theory*, 39:1213–1239.

Goyal, S., Ruina, A., and Papadopoulos, J. (1991a). Planar sliding with dry friction. Part 1. Limit surface and moment function. *Wear*, 143:307–330.

Goyal, S., Ruina, A., and Papadopoulos, J. (1991b). Planar sliding with dry friction. Part 2. Dynamics of motion. *Wear*, 143:331–352.

Haug, E. J., Wu, S. C., and Yang, S. M. (1986). Dynamics of mechanical systems with Coulomb friction, stiction, impact and constraint addition-deletion theory. *Mechanism and Machine Theory*, 21:365–446.

Howe, R. D. and Cutkosky, M. R. (1996). Practical force-motion models for sliding manipulation. *International Journal of Robotics Research*, 15(6):557–572.

Hunt, K. H. and Crossley, F. R. E. (1975). Coefficient of restitution interpreted as damping in vibroimpact. *Journal of Applied Mechanics*, 42:440–445.

Izmailov, A. F. and Solodov, M. V. (2008). An active-set Newton method for mathematical programs with complementarity constraints. *SIAM Journal on Optimization*, 19(3):1003–1027.

Jia, Y.-B., Mason, M. T., and Erdmann, M. A. (2013). Multiple impacts: A state transition diagram approach. *International Journal of Robotics Research*, 32(1):84–114.

Johnson, K. L. (1985). *Contact Mechanics*. Cambridge University Press.

Keller, J. B. (1986). Impact with friction. *ASME Journal of Applied Mechanics*, 53(1):1–4.

Klavins, E. (2007). Programmable self-assembly. *Control Systems Magazine*, 27(4):43–56.

Kraus, P. R., Fredriksson, A., and Kumar, V. (1997). Modeling of frictional contacts for dynamic simulation. In *Proceedings of IROS 1997 Workshop on Dynamic Simulation: Methods and Applications*, Grenoble, France.

Kry, P. G. and Pai, D. K. (2003). Continuous contact simulation for smooth surfaces. *ACM Transactions on Graphics*, 22(1):106–129.

Liu, T. and Wang, M. Y. (2005). Computation of three-dimensional rigid-body dynamics with multiple unilateral contacts using time-stepping and Gauss-Seidel methods. *IEEE Transactions on Automation Science and Engineering*, 2(1):19–31.

Miller, A. T. and Allen, P. K. (2000). GraspIt!: A versatile simulator for grasp analysis. In *Proceedings ASME International Mechanical Engineering Congress and Exposition*, pages 1251–1258, Orlando, FL.

Mirtich, B. (1996). *Impulse-based Dynamics Simulation of Rigid Body Systems*. PhD thesis, University of California, Berkeley.

Montana, D. J. (1998). The kinematics of contact and grasp. *International Journal of Robotics Research*, 7(3):17–32.

Murray, R. M., Li, Z., and Sastry, S. S. (1994). *A Mathematical Introduction to Robotic Manipulation*. CRC Press, Boca Raton, FL.

Nguyen, B. and Trinkle, J. C. (2010). Modeling non-convex configuration space using linear complementarity problems. In *IEEE International Conference on Robotics and Automation*, pages 2316–2321, Anchorage, AK.

Pang, J.-S. and Facchinei, F. (2003). *Finite-Dimensional Variational Inequalities and Complementarity Problems (I)*. Springer Verlag, New York.

Pauly, M., Pai, D. K., and Guibas, L. J. (2004). Quasi-rigid objects in contact. In *ACM SIGGRAPH/Eurographics Symposium on Computer Animation*, pages 109–119.

Pfeiffer, F. and Glocker, C. (1996). *Multibody Dynamics with Unilateral Constraints*. John Wiley, New York.

Ralph, D. (1994). Global convergence of damped Newton's method for nonsmooth equations via the path search. *Mathematics of Operations Research*, 19(2):352–389.

Rockafellar, R. T. (1970). *Convex Analysis*. Priceton University Press.

Routh, E. T. (1905). *Dynamics of a System of Rigid Bodies*. Macmillan & Co.

Seghete, V. and Murphey, T. (2010). Variational solutions to simultaneous collisions between multiple rigid bodies. In *2010 IEEE International Conference on Robotics and Automation (ICRA)*, pages 2731–2738.

Seghete, V. and Murphey, T. (2012). Conditions for uniqueness in simultaneous impact with application to mechanical design. In *2012 IEEE International Conference on Robotics and Automation (ICRA)*, pages 5006–5011.

Software, M. (2012). MSC Adams multibody dynamics software. http://www.mscsoftware.com/Products/CAE-Tools/Adams.aspx.

Song, P., Kraus, P., Kumar, V., and Dupont, P. (2001). Analysis of rigid-body dynamic models for simulation of systems with frictional contacts. *ASME Journal of Applied Mechanics*, 68(1):118–128.

Song, P. and Kumar, V. (2003). Distributed compliant model for efficient dynamic simulation of systems with frictional contacts. In *ASME Design Engineering Technical Conferences and Computers and Information in Engineering Conference*.

Song, P., Pang, J.-S., and Kumar, V. (2004a). A semi-implicit time-stepping model for frictional compliant contact problems. *International Journal for Numerical Methods in Engineering*, 60:2231–2261.

Song, P., Trinkle, J. C., Kumar, V., and Pang, J.-S. (2004b). Design of part feeding and assembly processes with dynamics. In *IEEE International Conference on Robotics and Automation*, pages 39–44, New Orleans, LA.

Stewart, D. E. and Trinkle, J. C. (1996). An implicit time-stepping scheme for rigid body dynamics with inelastic collisions and Coulomb friction. *International Journal of Numerical Methods in Engineering*, 39:2673–2691.

Trinkle, J., Pang, J., Sudarsky, S., and Lo., G. (1997). On dynamic multi-rigid-body contact problems with Coulomb friction. *Zeitschrift für Angewandte Mathematik und Mechanik*, 77(4):267–279.

Trinkle, J. C. and Pang, J. S. (1997). Dynamic multi-rigid-body systems with concurrent distributed contacts. In *IEEE International Conference on Robotics and Automation*, pages 2276–2281, Albuquerque, NM.

Trinkle, J. C., Ram, R. C., Farahat, A. O., and Stiller, P. F. (1993). Dexterous manipulation planning and execution of an enveloped slippery workpiece. In *IEEE International Conference on Robotics and Automation*, volume 2, pages 442–448.

Trinkle, J. C., Tzitzouris, J., and Pang, J. S. (2001). Dynamic multi-rigid-body systems with concurrent distributed contacts: Theory and examples. *Philosophical Transactions on Mathematical, Physical, and Engineering Sciences, Series A*, 359(1789):2575–2593.

Tzitzouris, J. A. (2001). *Numerical resolution of frictional multi-rigid-body systems via fully implicit time-stepping and nonlinear complementarity*. PhD thesis, The John Hopkins University.

Vose, T. H., Umbanhowar, P., and Lynch, K. M. (2009). Friction-induced velocity fields for point parts sliding on a rigid oscillated plate. *International Journal of Robotics Research*, 28(8):1020–1039.

Wang, Y. T. and Kumar, V. (1994). Simulation of mechanical systems with unilateral constraints. *ASME Journal of Mechanical Design*, 116(2):571–580.

Zumel, N. B. and Erdmann, M. A. (1996). Nonprehensible two palm manipulation with non-equilbrium transitions between stable states. In *IEEE International Conference on Robotics and Automation*, pages 3317–3323, Minneapolis, MN.